Localized Programmable Gas Phase Electrodeposition and Its Applications in Functional Nanomaterials and Devices

A DISSERTATION
SUBMITTED TO THE FACULTY OF THE GRADUATE SCHOOL
OF THE UNIVERSITY OF MINNESOTA
BY

Jun Fang

IN PARTIAL FULFILLMENT OF THE REQUIREMENTS
FOR THE DEGREE OF
DOCTOR OF PHILOSOPHY

Advisor: Heiko O. Jacobs
Co-Advisor: Bethanie Stadler

April 2016

Acknowledgments

The pursuit of a Ph.D. in Electrical Engineering at the University of Minnesota has been a great challenge for me over the past five and a half years. I would not have been able to complete this journey without the aid and support of countless people. While I am thankful to everyone who has helped me through the unfamiliar concepts and the late nights of experiments, there are some specific individuals whose contributions have been particularly significant.

First of all, I would like to thank my doctoral advisor Professor Heiko O. Jacobs for guiding my research over the entirety of graduate school. I have acquired a great deal of both knowledge and skill under his guidance. Professor Jacobs taught me how to conduct exploratory research in a professional setting. He also continually challenged me by regularly looking at results from a unique perspective and by finishing experimental setups using existing tools. I would also like to thank my doctoral committee members, Professor Beth Stadler, Professor Sang-Hyun Oh, and Professor Rusen Yang for their time and effort in reviewing this work.

I would like to thank Jacobs' group members, including Se-Chul Park, Forrest Johnson, En-Chiang Lin, Robert Knuesel, Jesse Cole and Michael Motala. Brain storming and exchange ideas with coworkers have been an enjoyable part of my graduate career.

In addition, I would like to thank all of my friends. Being with you is always one of the most memorable moments met during my Ph.D. study.

Last but not least, I owe my greatest gratitude to my beloved parents who had supported me to begin this journey.

Abstract

This thesis focuses on development and application of a gas phase nanomaterial integration concept. We developed and demonstrated a novel gas phase electrodeposition method to control material flux transported and deposited at desired points on a patterned biased substrate based on the Coulomb force. The thesis is divided into two sections: (A) a corona based analyte charging method and an electrodynamic nanolens based analyte concentration concept to effectively transport airborne analytes to sensing points to improve the response time of existing gas sensor designs, and (B) a gas phase electrodeposition process to grow free-standing point-to-point electrical nanowire connections spanning a distance of up to 10 μm.

Section A introduces a new general approach which uses a corona based charging method in combination with an electrodynamic lens based collection concept to transport particles to precise points on a surface. We discovered that the transport is faster than diffusion based transport commonly used. The faster transport and speed was then applied to the field of nanosensors of airborne particles. Specifically, we were able to reduce the response time of existing airborne sensor designs by several orders of magnitude. The process, referred to as "corona/lens-based-collection", enables us to transport nanomaterials and airborne analytes from a space that is centimeters away to specific sensing points on a surface with a minimal spot size approaching 100 nm. We find that the collection rate is several orders of magnitudes higher than the case where the corona/lens-based-collection is turned off and collection is driven by diffusion only. The collection scheme is integrated on an existing SERS based sensor that is sensitive to the adsorption of small molecules. We compare the results with and without corona/lens-based-collection and find that SERS signal is enhanced by three orders of magnitudes as a result of increased collection efficiency. In terms of response time, the process is able to detect analytes at 9 ppm (parts per million) within 1 second. As a comparison, 1 hour is required to approach the same signal intensity in the case where diffusion-only-transport is used.

Section B presents a gas phase electrodeposition process to grow free-standing point-to-point electrical nanowire connections spanning a distance of up to 10 μm. The gas phase electrodeposition process uses a patterned resist with openings to a conductor to guide the deposition of charged nanoparticles. Nanowire growth occurs at charge dissipating contacts which are accessible due to the openings in the resist. The formation of interconnects between contacts or bridges across a trench is possible through nearest neighbor interaction. The growing nanowires are composed of metallic nanoparticles. We discovered that a reduction of the primary nanoparticles size to the 1-5 nm range is required to achieve electrical conductive and mechanically stable bondwires. The annealing temperature has been reduced to 250°C due to the small particle size. The diameter of the nanowires depends on the growth duration and the size of the openings. The adjustable range is 50 nm-1 μm. Mechanically stable bondwires have a typical diameter of 250 nm. A 5 μm long interconnects with a radius of 250 nm had a resistance of 85 Ω.

Table of Contents

List of Figures

CHAPTER I

CHAPTER III

CHAPTER IV

CHAPTER V

CHAPTER VI

List of Tables

CHAPTER III

CHAPTER IV

Chapter I

Motivation, Background and Project Introductions

Motivation

This thesis focuses on development and application of a gas phase nanomaterial integration concept. A novel gas phase electrodeposition method is demonstrated to control material flux transported and deposited at desired points on a patterned biased substrate based on the Coulomb force. Two major applications were discussed in this theis: (i) An corona based analyte charging method and an electrodynamic nanolens based analyte concentration concept to effectively transport airborne analytes to sensing points to improve the response time of existing gas sensor designs. [1, 2] We believe that this method will be of interest to a wide scientific audience since it is not limited to the chosen field. In the field of sensors that target the detection of airborne analytes, it provides a new path and view point to achieve high sensitivity and selectivity, which impacts research fields that range from environmental monitoring systems to the detection of chemical or biological warfare agents. Specifically, it provides a route to transport, concentrate and collect the airborne species to precise sensing points. (ii) A gas phase electrodeposition process to grow free-standing point-to-point electrical nanowire connections spanning a distance of up to 10 μm. The gas phase electrodeposition is applied to grow self-aligned free-standing nanowire based interconnects. [3] The interconnects can connect distant points with each other through the control of the dissipation current. The purposed idea enables the possibility to create truly 3D free-standing nanowire structures and freeform wire connection between disparate “off chip” parts of a system. The formation of vias between device layers through gas phase deposition should also be possible. [4]

Background

Jacobs' group have developed a localized gas phase electrodeposition system, [4-8] which is an electrodynamic Coulomb force directed nanomaterial transport process. The mechanism, as far as it is understood, is based on the interplay between (i) high mobility gas ions, (ii) lower mobility particles/molecules, (iii) a patterned substrate to shape the electric potential landscape and to guide the collection process, and (iv) a carrier gas. The process has been described in parts before. The relevant elements as it is known so far are briefly described to put the current research in context. First it is a localized material growth/deposition process which uses charged insulators to attract or deflect an incoming flux of charged material. This is illustrated in **Figure 1-1**, which compares the recently discovered gas phase electrodeposition process with conventional physical vapor deposition. The starting point in both methods is a patterned photoresist or e-beam resist. However, on the right side the material to be deposited (orange particles) is directed to the point of use and no material is lost in subsequent lift-off processes.

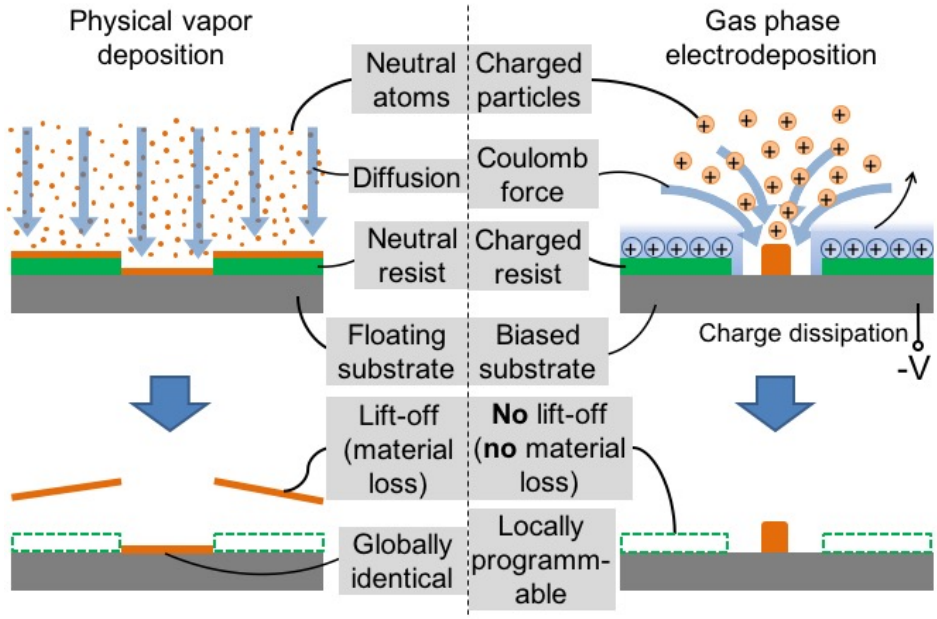

Figure 1-1: Comparison between conventional physical vapor deposition (left) and localized gas phase electrodeposition (right). Under steady state operation the charged particles deposit locally in the charge dissipating opening. The insulating resist (green layer) has acquired a static surface charge distribution which yields fringing fields

whereby the particles are funneled into the charge dissipating openings. No continued buildup of material on the insulating resist.

Taking a closer look at the basic process, it becomes clear that gas phase electrodeposition shares some of the characteristics of electrodeposition in the liquid phase. However, it is a gas phase process with a much larger mean free path of the particles. The Debye length representing the screening length of Coulomb forces is also larger. [5] Despite this difference, it can grow nanostructures in selected domains in a programmable fashion by adjusting the dissipation current of the ionic species that arrive at the surface. For example, in the simplest case it was used to grow straight metallic nanowire arrays whose height and density were adjusted to vary across the substrate which in turn were used as contacts in photovoltaic devices. [9] Others have used this technique to fabricate metallic nanostructures for surface enhanced Raman spectroscopy (SERS). [5, 6] In any event, charged material continues to deposit into locations where charge dissipation can occur, leading to a growth of extended structures much like what is observed in the liquid phase based electrodeposition/plating.

Project Introductions

Section A: Localized collection of airborne analytes: a transport driven approach with programmable ability to improve the response time of existing gas sensor designs (publication 1 and 2)

Introduction: Previously, the research group of Prof. Jacobs have developed a localized gas phase deposition concept, which uses a biased patterned substrate to collect and assemble charged nanoparticles at desired location at a lateral resolution that exceeds conventional patterning methods. [4, 5]

Based on the developed gas phase deposition concept, this research introduces a novel corona discharge based localized collection process to improve the response time of existing gas sensor designs. (**Figure 1-2**) The goal was to address the following problem:

(i) Nanostructured gas sensors currently aim for, or claim single molecular detection which is commonly achieved by a reduction of the active sensor size. Reported sensing schemes, however, use diffusion as a mechanism for transport which leads to the question of whether the analyte will ever find the nanometer sized area. [11-13] In other words, single molecular detection sensitivity is important but requires the molecule of interest to reach the sensing surface. This becomes increasingly unlikely unless methods are employed which enable localized analyte delivery. The reported collection process is a first step in this direction. Our approach is capable to direct airborne analytes over a wide range of molecular weights (from 3×10^{17} to 1×10^{2} Daltons) to localized sensing points. We introduce an addressable electrodynamic nanolens array to funnel and concentrate the analytes in discrete sensing points with 100 nm lateral resolution.

(ii) In order to detect and identify trace amounts of airborne analytes, it is usually required that the analyte is collected on the substrate (for OFFSITE detection) which brings up the question of how to transport an airborne analyte to the target surface. [14, 15] We use a directed force to efficiently collect and store analytes in an active matrix array like fashion, at predetermined points on a surface, at different points in times, which in turn provides a time record or memory of the events that occurred in the past yielding an average exposure, peak exposure, and exposure of various species on an as needed basis. [2]

The utility of the method is tested using a SERS based sensing standard. However, many other sensing modalities could be used as well. The results are impressive. The process is able to detect and identify airborne molecules at an estimated level of 9 ppm (parts per million) within 1 second; as a comparison, to achieve the same Raman signal level using a standard diffusion mechanism requires more than 1 hour. This record reduction in response time represents three orders of magnitudes. This result is particular relevant since the approach can be implemented in other sensing platforms leading to similar improvements.

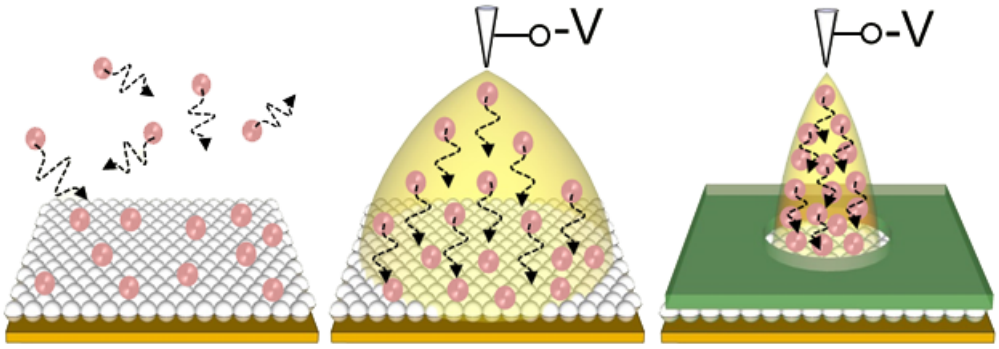

Figure 1-2: A schematic comparison of diffusion-based collection (left), corona-based collection (middle), and nanolens assisted corona-based collection (right). Corona discharge (yellow) is generated between a tip-to-plate structure and is used to charge the analyte particles (red) and the dielectric thin film (green) negatively, primarily through the attachment of electrons. Analyte collection and concentration occurs at predetermined charge dissipating sensing points.

Summary of Main Results: The response time of gas sensors has been greately improved using the directed transport schemes that have been introduced. It is not possible to detect such a low analyte concentration using the diffusion-only-transport standard unless a much longer exposure time is used. For example, it took a 1 hour long exposure using diffusion-only-transport to achieve the same signal intensity level. The approach should benefit any sensing concept that involves a surface sensor and not just SERS. What it means is that others adapting this concept should anticipate several orders of magnitude increases in response time over sensing systems that use diffusion-only-transport to the surface sensor they use. In addition, the ability to direct analytes to nanoscopic sensing points using the nanolens is relevant in light of recent research on nanosensors, where a trend has been to shrink down the active sensor area to a point to detect single molecular binding events. While this trend increased the sensitivity, it came at the price of a slow response time since it is increasingly unlikely for a molecule to "find" the nanoscopic sensing elements/points using the diffusion-only-transport, as impingement and capture rates scales with the area of the sensing element. As a consequence, the introduced nanolens based transport can be employed to increase the collection speed and localized concentration of the analyte on nanoscopic sensing elements to acceptable levels.

The application of the discovered process as an active matrix analyte recording chip has been limited by the number of electrical connections that we can make. From a practical point of view, a multiplexing concept would have to be introduced to further increase the number of isolated recording sites. From a physical point of view, however, it should be possible to achieve a larger number of recording sites than what has been demonstrated. Specifically, the analyte transport based on random diffusion was 400 to 1000 times slower than the directed transport method used in this study. This means that it should be possible to record a sequence of 400 to 1000 analyte exposures before diffusion based cross-contamination becomes the limiting factor. The basic idea is that such a chip could be a commodity item that is placed in an environment that a user would like to keep a record from. The information is retrieved on an as needed basis. Offsite analysis of the chip storing the information would make this approach more economical than an online monitoring system for all kinds of threads.

Section B: Self-Aligned Growth of Freestanding Nano-Bridge-Based Interconnects (Publications 3 and 4)

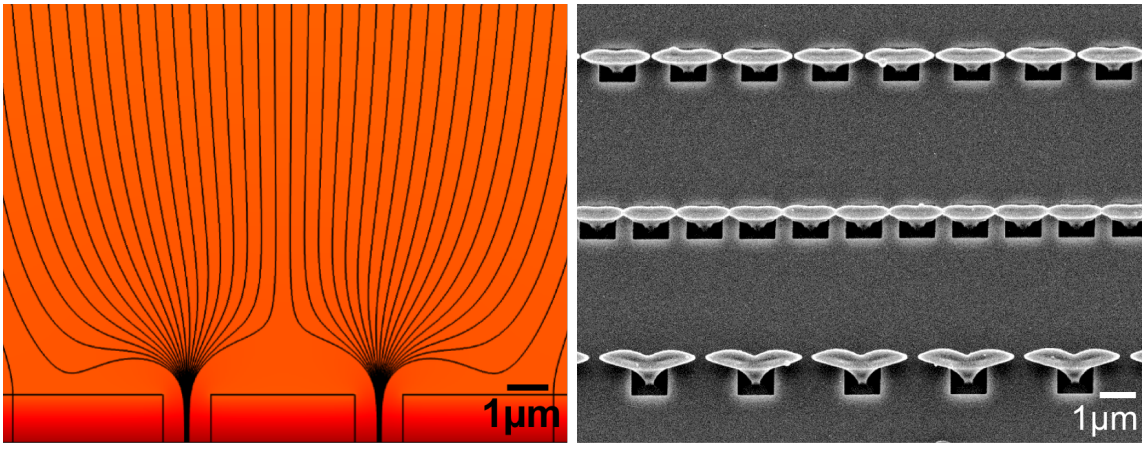

Figure 1-3: Nearest neighbor interaction: computed electric field distribution at two nearby openings with 1 µm thick photoresist (left) and the formation of copper bridges between nearest neighbors (right).

Introduction: This section will explore the application of gas phase electrodeposition from a different perspective. An interesting discovery deals with the screening length and nearest neighbor interaction of electric fields. In the wet chemical electrodeposition, the

Debye length is often used as measure to determine the screening length. It is commonly smaller than 10 nm and nearest neighbor interaction is limited. This is different in the discovered gas phase electrodeposition process. Nearest neighbor interaction can take place at much larger distances (10 µm in some cases). This supports a different set of applications. **Figure 1-3** provides some understanding on the effect of nearest neighbor interaction comparing computed electric field distributions with deposition results using a 1 µm thick photoresist with 1 µm sized openings to a Si substrate. From a computation point of view, an increase in the surface potential leads to: (i) an increased focus of the electric field lines and (ii) fewer field lines which impinge on the insulating resist surface. The depicted impinging field lines are present at the outset of the experiment. A 1 µm thick layer of Microposit S1813 has a breakdown strength of ~400 V/µm and can thus float up to a sufficiently high value to divert the flux of charged particles. The process is capable to grow free-standing point-to-point electrical connections using metallic wires with diameters down to 200 nm spanning a distance of up to 5 µm in the present form. The registration between contact pads is based on a self-alignment process. Registration to sub 1 µm wide contact pads is possible. The nanowire bonding process [16] is based on a method that is best referred to as "gas phase electrodeposition". [6, 8] It is a new localized material growth/deposition process which uses charged insulators to attract [17] or deflect [18] an incoming flux of charged particles and gas ions. A goal of this study was to realize electrically conducting structures and interconnects in a self-aligned fashion and some of the key parameters to achieve this goal have been identified. These parameters include the material flux, carrier gas flow rate, and the primary particle size. Two types of operation regimes will be discussed: a (i) "low-carrier-gas-flow regime" which produces dendritic high surface-to-volume ratio structures and a (ii) "high-carrier-gas-flow regime" where defined and dense metallic nanowires are formed. The application of the tool as a nanowire bonding process required the formation of mechanically and electrically stable interconnects. This was only possible if the nanowires were composed of densely packed nanoparticles where the primary particle size was reduced to the 1-5 nm range.

Summary of Main Results: We discovered a nearest neighbor coupling effect which supports the growth of bridges. The growth of bridges is possible due to an increased screening length when compared to the wet chemical counterpart where a high ion

concentration screens charges within a few nm. Nearest neighbor coupling across a 10 μm gaps is possible. This finds applications. The gas phase electrodeposition is applied to grow self-aligned free-standing nanowire based interconnects. The interconnects can connect distant points with each other in a programmable fashion through the control of the dissipation current. The formation and self-aligned growth is also used to grow an interdigitated electrode array. Here nanowire bridges grow across the rows and columns. No electrical shorts between the columns and rows were detected indicating that the crossovers are not in contact with the electrodes underneath. In the future it should be possible to extend this further. It is possible to create turly 3D free-standing nanowire structures and freeform wire connection between disparate “off chip” parts of a system. The formation of vias between device layers through gas phase deposition should also be possible.

Chapter II

Introductory Note

The following chapters present four articles that have been published in pair reviewed journals with the exception of article 4 which has been submitted:

Chapter III (Publication 1, published) addresses a localized collection of airborne analytes concept to improve the response time of existing gas sensors.

Chapter IV (Publication 2, published) addresses an active matrix based analyte collection method to provide exposure history and finger print of the analyte.

Chapter V (Publication 3, published) addresses a gas phase electrodeposition concept to enable the self-aligned growth of 3D nano-bridge-based interconnects.

Chapter VI (Publication 4, submitted) addresses the growth of free-standing point-to-point electrical connections and microscopic bondwires based on gas phase electrodeposition.

Chapter III

Localized Collection of Airborne Analytes: A Transport Driven Approach to Improve the Response Time of Existing Gas Sensor Designs

Jun Fang, Se-Chul Park, Leslie Schlag, Thomas Stauden, Jörg Pezoldt, and Heiko O. Jacobs

***Adv. Funct. Mater. 24**, 3706 (2014)*

3.1 Introduction

The desire to detect and identify trace amounts of airborne analytes, including combustible or toxic gases, small molecules, particles, viruses or bacteria with ever increasing sensitivity and selectivity continues to be one of the main drivers in sensor research. [19-21] While the variety of sensing principles continues to grow, most principles share a common feature which is the requirement that the analyte adsorbs on the sensor surface or interacts chemically or physically with the sensing element for signal transduction to take place. For example, adsorption and analyte interaction is critical in sensors that use an electrochemically active surface, [11] surface catalysis, [12] a mesoporous metal-semiconductor-metal network, [13] a chemically sensitive field effect transistor, [22] a resonant mechanical beam, [23] or optical methods such as fluorescence microscopy [24] and SERS (surface-enhanced Raman spectroscopy), [10, 25, 26] to name a few. A recent trend has been to increase the sensitivity to a point where it is possible to detect single binding events. Here the common approach has been to reduce the active sensor size, for example using nanometer sized transistors, [24] resonating cantilevers, [27] surface plasmons, [15] and nanogaps. [28] While it is possible to detect single binding events through the introduction of these highly miniaturized sensing points, the efficient transport of the airborne analytes to point-like structures has been a critical factor to improve the response time. Commonly, transport is driven by diffusion which is not the best approach. Specifically, basic gas laws provide a simple formula to calculate the number of analyte particles that impinge on a surface

$$N = R_i \cdot A \cdot \Delta t = \frac{8.33 \cdot 10^{22} \cdot P_i}{\sqrt{T \cdot M}} \cdot A \cdot \Delta t \qquad (1)$$

where R_i is impingement rate (number·m^{-2}·s^{-1}), P_i is partial pressure (Pa) of the analyte in a gas mixture which increases with its concentration, T is temperature (K), M is its molar mass (kg/mol), A is sensing area exposed to the analyte (m^2), and Δt is exposure time (s). Considering Equation 1 there is a downside when the active sensor size is reduced to an extremely small value since the total number of analyte particles that actually interact with a point-like sensing structure approaches zero. In other words, it becomes increasingly

unlikely for an analyte molecule to "find" and interact with an ever increasingly small sensor, trading an increased sensitivity with a slow response time.

Instead of relying on diffusion-only-transport, this report evaluates the use of a directed force to overcome this problem and to transport the analyte from a distance away to predetermined sensing points at a higher rate. The approach is inspired in part by prior research in the aerosol community which has developed transport strategies to collect airborne particles using convection, [29] thermophoretic, [30] magnetic, [31] and Coulomb forces. [4, 32] Among these candidates, Coulomb force based concepts have found a wide range of applications ranging from the collection of dust particles in air purifier and electrostatic filters [33] to the manipulation of molecules in mass spectrometry. [34] Most of these precipitation concepts including a cold substrate (thermophoretic) [30] or an electrically biased metal plate (electrostatic precipitator) [4, 35] collect the materials over a relatively large surface and effective localized collection on nanoscopic sensing points has not yet been reported. One exception but outside of the field of sensors is employed in Xerographic and Nanoxerographic printers [5, 18] which use a charge patterned surface to attract nanoparticle locally as supposed to globally. Particular the recently gained knowledge in the field of Nanoxerography [6, 8] is relevant since it has become evident that localization of nanoparticles is possible with sub 100 nm lateral resolution. While the application was in the field of printable electronics it inspired the presented research to evaluate if it is possible to employ similar schemes to the field of sensing of airborne species including small molecules. As a results this article reports and applies a localized electrodynamic precipitation concept to collect, spot and detect airborne species in predetermined locations with sub 100 nm lateral resolution, which can further concentrate the analytes and improve the response time of prior results. Specifically, we introduce a new general approach which uses a corona discharge based analyte charging method in combination with an electrodynamic lens based analyte collection concept to transport airborne analytes to precise points on a surface to improve the response time of existing gas sensor designs by several orders of magnitude. The process, referred to as "corona/lens-based-collection", enables us to transport analytes from a space that is centimeters away to specific sensing points on a surface with a minimal spot size approaching 100 nm. The approach is widely applicable demonstrating localized collection of (i) microscopic

particles (Kentucky blue grass pollen, 20 µm in diameter, ~3×10^{17} Dalton), (ii) inorganic nanoparticles (CdSe nanoparticles, 4 nm in diameter, ~1.4×10^{5} Dalton), all the way down to (iii) small organic molecules (Alq_3, 459.43 Dalton; anthracene, 178.23 Dalton; benzenethiol, 110.19 Dalton). In all cases we find that the collection rate is several orders of magnitudes higher than in the case where the corona/lens-based-collection is turned off and where collection is driven by diffusion only. To demonstrate and quantify how this general strategy improve the response time of an existing gas sensor design, the collection scheme is integrated on an existing SERS based sensor that is sensitive to the adsorption of benzenethiol. The particular SERS sensor employs the standardized AgFON (Ag film over nanosphere) substrate. We compare the results with and without corona/lens-based-collection and find that SERS signal is enhanced by three orders of magnitudes as a result of increased collection efficiency. In terms of response time, the process is able to detect analytes at 9 ppm (parts per million) within 1 second. As a comparison, 1 hour is required to approach the same signal intensity in the case where diffusion-only-transport (current standard) is used. The report also addresses the question of concentration ratio as a function of lens diameter whereby smaller diameters increase the concentration ratio.

3.2 Results

3.2.1. Corona/Lens-Based-Collection Procedure

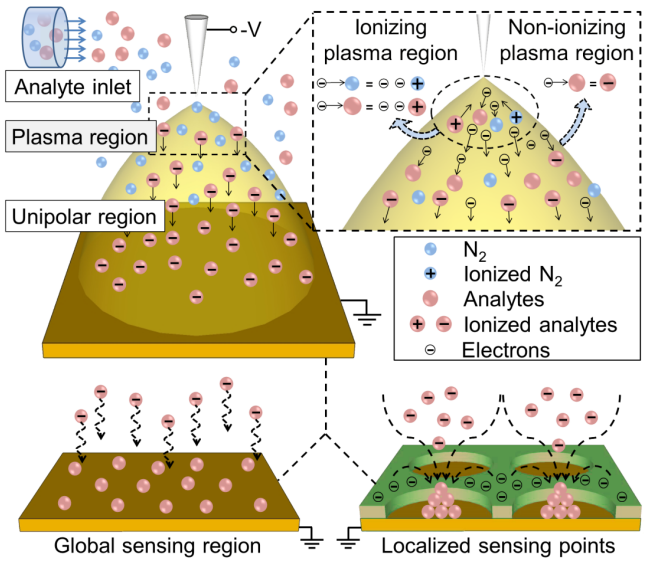

Figure 3-1. Schematic of advanced analyte transport and collection using corona discharge in combination with an electrodynamic lens based concentrator. Uniform collection across an extended charge dissipating sensor surface (bottom left) is extended to localized concentration and collection (bottom right) using a negatively charged dielectric. Corona discharge is used to charge the analyte particles (red) and the dielectric thin film (green) negatively, primarily through the attachment of electrons (insert). The depicted fringing field is a consequence of the buildup of surface charge and acts as an electrodynamic funnel. Analyte collection and concentration occurs at predetermined charge dissipating sensing points. The term "surface sensor" is used as a placeholder for all types of sensors that require analyte transport and adsorption on a sensing surface for signal transduction to take place.

Figure 3-1 describes the procedure of corona/lens-based-collection. The airborne analyte enters the system from the left. When compared to conventional point to conducting plate corona discharge experiments, [36] this report adds a patterned dielectric thin film with openings to the conductive plate to form a single or arrays of lensing structures. The purpose of the introduced dielectric lensing structures is to provide an electrodynamic funnel to transport the analyte from a distance away to desired sensing points on a surface with sub 100 nm placement accuracy. The purpose of the corona based charging system is to achieve a high degree of charging, which in combination with the electrodynamic lens based transport, increases the localized collection rate of the analyte far beyond levels reported so far. Depicted is the case where the analyte (red dots) is surrounded by N_2 (blue dots) which unless stated otherwise represents the carrier gas we used. From an analyte collection point of view we compared two designs: (i) one where the collection is uniform across extended surface region (global sensing region, bottom left) and (ii) one where the analyte is delivered to certain sensing points (localized sensing points, bottom right). The delivery to certain sensing points involves the introduction of electrodynamic lens arrays which are defined by a patterned dielectric layer (green) with openings to a charge dissipating sensing device layer. The actual dimensions will be discussed later. To charge and transport the analyte to predetermined locations, a corona discharge surrounding a pointed electrode is used. [37, 38] In brief, positive ionization occurs within a fairly thin ionizing plasma region, [36] where the electric field is

sufficiently strong to cause the emission of electrons through the photoelectric effect which subsequently produce positive gaseous species and secondary electrons through impact ionization. [37] Beyond this region, the electric field diminishes rapidly and electrons with energy lower than ionization energy will attach to neutral analyte yielding negatively charged analyte particles (non-ionizing plasma region). These negatively charged species move downwards through the depicted unipolar region (negative) until they reach the grounded or positively biased sensing structures. In the case where the dielectric layer is introduced, the dielectric becomes negatively charged through the deposition of electrons. The subsequent buildup of charge leads to the depicted fringing field which under steady state condition diverts the charged analyte to the desired charge dissipating sensing points. [5] These predetermined sensing points can hold any conductive surface sensor including a SERS sensor discussed later.

3.2.2. Corona/Lens-Based-Collection of Various Analytes

Figure 3-2 provides a CAD drawing of the collection chamber and micrographs of the samples testing the collection of various analytes ranging from 3×10^{17} to 1×10^{2} Dalton. In the depicted set of experiments, optical, fluorescence and scanning electron microscopy was used as a detection method to provide a visual response of the analyte distribution. All analyte collection experiments use the collection chamber depicted in (a) which was machined out of an insulating acrylic block to provide a 3cm×3cm×3cm cavity, a 10 mm in diameter gas inlet, a 3 mm in diameter gas outlet, a pointed copper electrode 5 mm above the sample, a sample port and a sample tray. In the particular set of experiments, periodic electrodynamic lens arrays were used. The lens arrays are defined using a patterned 500 nm thick layer of insulating photoresist (s1805, Microposit™) with 200 μm square (b) or 1 μm circular (c-g) openings to a flat silicon substrate. All chips were 5 mm wide and 10 mm long. All analytes were introduced to the testing chamber using 2000 sccm (standard cubic centimeters per minute) of N_2 as a carrier gas. The SEMs and optical/fluorescent micrographs illustrate the range of analyte particles that can be collected. Specifically, we tested gas mixtures (aerosols) containing large microscopic particles Kentucky blue grass pollen (20 μm in diameter, ~3×10^{17} Dalton, b), fluorescent CdSe nanoparticles (4 nm in diameter, ~1.4×10^{5} Dalton, c), all the way down to small molecules such as fluorescent

Alq_3 (459.43 Dalton, d), fluorescent anthracene (178.23 Dalton, e), non-fluorescent tobacco smoke (nicotine, tar, etc., f), and non-fluorescent benzenethiol (110.19 Dalton, g).

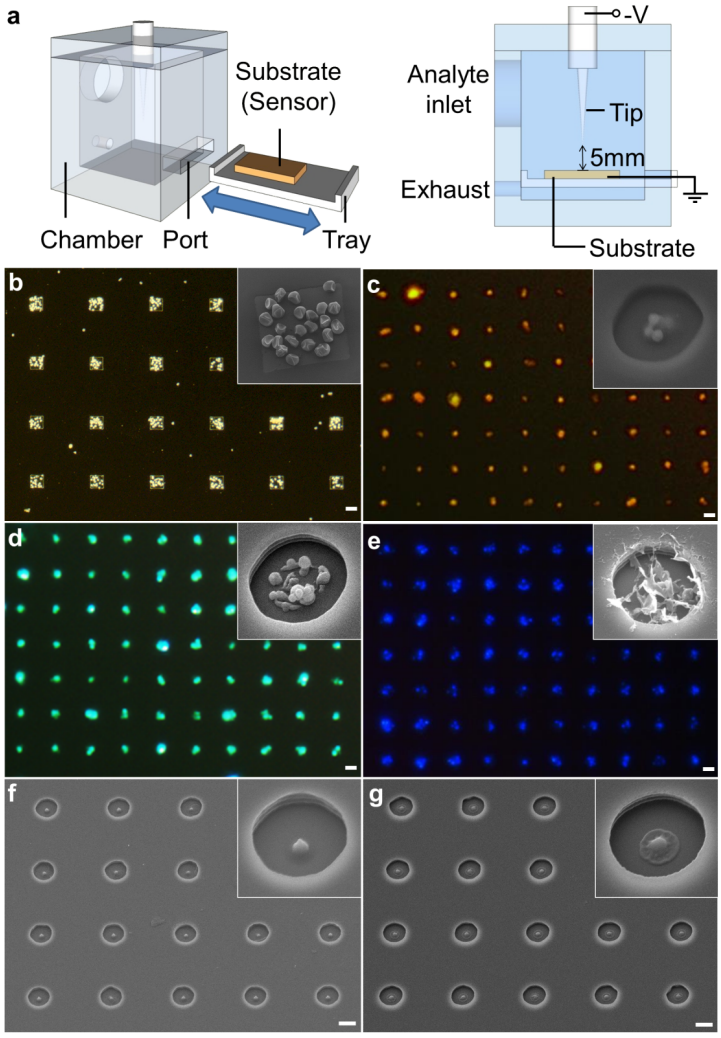

Figure 3-2. *A CAD drawing of the collection chamber and micrographs of corona/lens-based-collection of various analytes representing a wide range of molecular weights (from 3×10^{17} to 1×10^{2} Dalton). (a) Insulating acrylic chamber with gas inlet, gas outlet, pointed electrode, sample port and sample tray. (b) Optical microscope image of locally collected Kentucky blue grass pollen. (c-e) Fluorescent microscope images of locally collected CdSe quantum dots, Alq_3 and anthracene. (f-g) SEM images of locally collected tobacco smoke and benzenethiol. Inserts show SEM closeups. The scale bars are 200 μm in (b) and 1 μm in (c-g).*

From an experimental point of view, the following general observation were made: First, independent of analyte type or size, it is possible to transport, concentrate, and collect the various analytes at predetermined sensing points using the introduced corona/lens-based-collection process which is remarkable considering the large range of analytes we tested. In terms of molecular weight, the results represent a range of 3×10^{17} to 1×10^{2} Dalton. Second, the structures and at least some of the relevant physical properties remain intact. For example: (i) shape of the pollen particles; (ii) fluorescent characteristics of the CdSe quantum dots, Alq_3 molecules and anthracene molecules; and (iii) spectral response due to Raman scattering (detailed later), remain intact. Third, the localized collection rate is large compared to the commonly used approach where the particles deposit randomly on the surface by diffusion-only-transport. In the case of benzenethiol, discussed in more detail below, the collection rate was determined to be 3 orders of magnitude faster than diffusion. This is remarkable since it means that the response time in a sensor application will be improved. The faster transport and concentration reduce the required collection time from hours to seconds. In the depicted results 5 seconds was used for CdSe quantum dots and Alq_3 and 1 second for the remaining samples. To reach such short exposures times it was necessary to use a special chamber design depicted in (a) which uses a sample tray that can be shifted back and forth between two sealed positions. In the particular design the corona discharge occurs only as the grounded sample is shifted to the exposure position which is underneath the negatively biased -5 kV tip electrode. Moreover, we monitored the actual exposure current and time using an oscilloscope that measures the voltage drop across a 1 kΩ resistor that is connected in series with the high voltage source. The discharge currents were 1300, 260, 380, 1000, 125, 600 μA in the case of pollen, CdSe quantum dots, Alq_3, anthracene, tobacco smoke, benzenethiol, respectively.

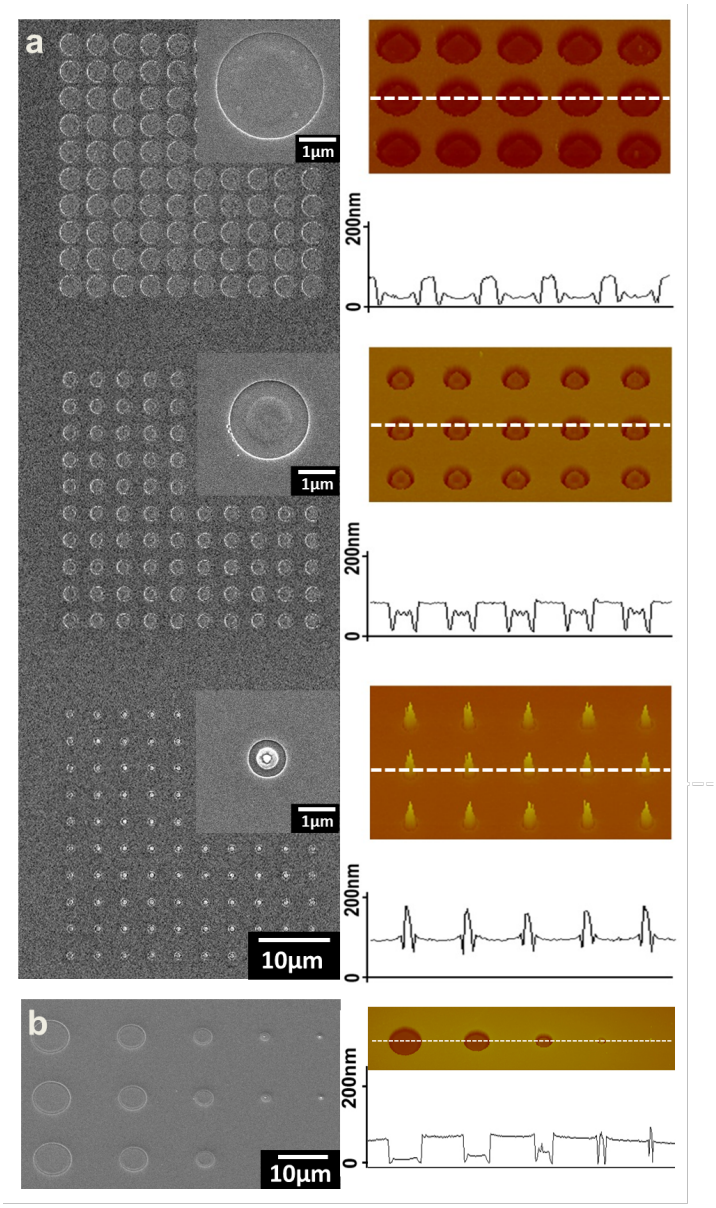

Figure 3-3. Behavior of analyte concentration as a function of opening size and pitch. (a) SEM images (left) and corresponding AFM topography scans (right) showing localized collection of benzenethiol using 10×10 arrays of 90 nm deep wells on a 4 µm pitch with 3 µm, 2 µm and 1 µm diameter openings and corresponding 25 nm, 57 nm, 180 nm analyte collection height. (b) SEM image (left) and AFM topography scans (right) of a different region with 8 µm, 6 µm, 4 µm, 2 µm and 1 µm diameter openings. In the tested range, the observed analyte concentration factor is roughly inversely proportional to the opening area.

The locally collected analyte amount is found to be related to the diameter and pitch of the lens forming elements. **Figure 3-3** presents results to investigate the amount of analyte as a function of opening size and pitch. The images show SEM micrographs (left) next to corresponding AFM topography scans (right) of a sample exposed to a benzenethiol gas mixture containing 9 ppm benzenethiol in N_2 for 1 second. The depicted nanolens arrays in this study were prepared using an e-beam lithography patterned 90 nm thick layer of PMMA with circular openings (3 µm, 2 µm and 1 µm in (a) and 8 µm, 6 µm, 4 µm, 2 µm and 1 µm in (b)) on a silicon substrate. Generally, we find that the locally collected analyte amount increases with a reduced opening size. In the illustrated Figure 3-3 (a) the thickness of the precipitates increases from 25 nm, to 57 nm, to 180 nm with 3 µm, 2 µm, and 1 µm openings, respectively. **Table 3-1** provides a more detailed analysis of the AFM data and provides the average diameter, height, and volume of the precipitates in the three regions. Interestingly, in terms of volume each point collects about the same material. In other words, a constant material flux is "squeezed" into exceedingly small areas yielding tall structures containing the analyte. All patterns we have tested so far followed this general trend. The material concentration factor is roughly inversely proportional to the opening, which means that it is possible to adjust the concentration ratio and consequently response time in a gas sensor application to a desired value.

Table 3-1. Average precipitation amount collected in 1 second in terms of diameter, height, and volume based on Figure 3-3 (a).

Region / **Precipitate**	**Ø 3 μm openings**	**Ø 2 μm openings**	**Ø 1 μm openings**
Diameter [μm]	2	1.2	0.7
Height [nm]	25 (36 monolayers)	57 (81 monolayers)	180 (257 monolayers)
Volume [μm^3]	0.079	0.064	0.069

The case of the benzenethiol is particular interesting for further studies since it is substantially different from the other analytes we tested. The CdSe quantum dots, Alq_3,

and anthracene are fluorescent substances that simplified the detection which is not the case for benzenethiol. The benzenethiol is the smallest analyte in the test series. Most importantly it is a liquid at room temperature (vapor pressure: 1.4 mmHg at 300 K). However, the recorded precipitates discussed in Figure 3-3 were solid which means that the substance cannot be pure benzenethiol. The recorded deposits formed as a result of exposure to a gas mixture containing 9 ppm benzenethiol in N_2. However, this does not completely eliminate the potential of oxidation. Moreover, the samples are exposed to air for further characterization. In air benzenethiol decomposes and produces sulfur oxides, biphenyl, diphenyl sulfide and dibenzenethiophene, [39] which are all solids at room temperature; such reactions are not integral part of the collection process presented here since they will occur in a diffusion-only-transport as well. Nevertheless, it is interesting since it raises the question of whether or not benzenethiol is present in the precipitates which will be evaluated in the following section where we integrate the localized transport mechanism with a SERS based gas sensor.

3.2.3. Corona Discharge Driven Transport Integrated on an Existing SERS Gas Sensor --Response Time Improves by Three Orders of Magnitude

The following section demonstrates and quantifies how this general strategy improves the response time of an existing gas sensor design. Specifically, we integrated the collection scheme on an existing SERS based sensor that is sensitive to benzenethiol. As far as we know, prior SERS based gas sensors used diffusion to transport the analyte to the sensing surface. **Figure 3-4** compares the corona-based-collection scheme with the diffusion-only-transport (current standard) in case of a SERS sensor and shows schematics of the testing conditions (top), next to corresponding Raman microscopy intensity maps at 1573 cm^{-1} (middle), and resulting spectra (bottom). The particular SERS sensor employs an AgFON substrate, which is considered the standard in the field of SERS detection. In brief, the AgFON surface enhancing layer is a closely packed self-assembled layer of 200 nm in diameter silica nanospheres where the top half is coated with 20 nm/180 nm Cr/Ag film. To maintain the original state of the AgFON surface the collection concept was first tested without the integration of the dielectric lensing structures discussed before. Instead it used only the corrugated nanostructured Cr/Ag film. This film supports the application of the

required voltage between the pointed electrode and the substrate and no additional modifications are necessary. All substrates were 5 mm wide and 10 mm long. Analog to prior experiments we used the 9 ppm of benzenethiol in N_2; prepared using 10 sccm of N_2 flowing through a benzenethiol containing bubbler further diluted using 2000 sccm of N_2. The Raman intensity at 1573 cm^{-1} was recorded under four exposure conditions: (a) 1 second long exposure using diffusion-only-transport yielding 1-2.5 counts (red, 2 was used in the relative comparison), (b) 1 second long exposure using corona-based-collection under -4 kV (135 µA) yielding 230 counts (blue, 115 times more), (c) 1 second long exposure using corona-based-collection under -5 kV (450 µA) yielding 570 counts (green, 285 times more), and (d) 1 hour long exposure using diffusion-only-transport yielding 470 counts (black, 235 times more).

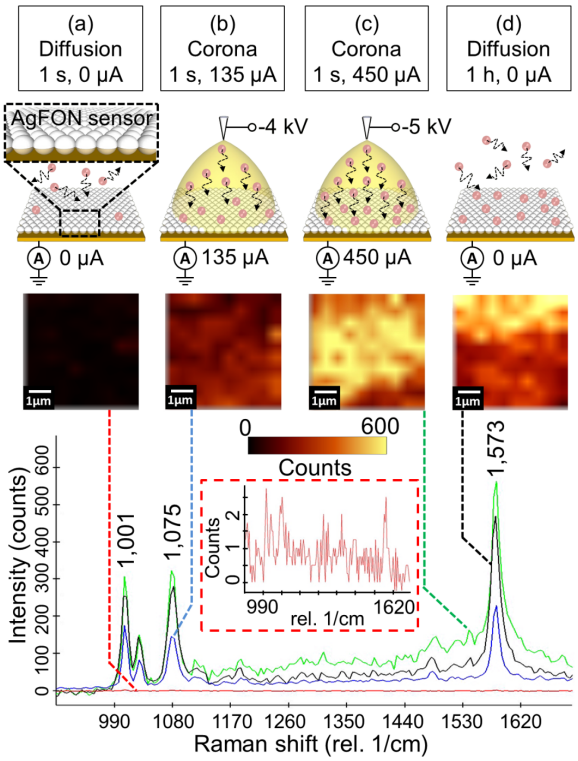

Figure 3-4. SERS sensor comparing diffusion-only-transport with corona-based analyte collection, illustrating schematics of the testing conditions (top), next to corresponding Raman microscopy intensity maps at 1573 cm^{-1} (middle), and resulting spectra (bottom): (a) diffusion-only-transport with 1 second long exposure, Raman intensity is close to zero and an insert provides details; (b) corona-based-collection (-4 kV) with 1 second long

exposure; (c) corona-based-collection (-5 kV) with 1 second long exposure; (d) diffusion-only-transport with 1 hour long exposure. Raman intensity maps show raw unprocessed data recorded at 1573 cm^{-1} using the same microscope settings. Raman spectra represent an average recorded by the instrument over a 5µm×5µm sized region; an offset (up down) correction has been applied for the spectra to overlap at the beginning of the graph; peak height measurement and relative comparison is not effected.

Using diffusion-only-transport the collection rate is fastest in the beginning (a few counts per second) and slows down over time following a time-dependent Langmuir kinetics approximated by $500\ counts\times(1-e^{-\frac{t}{18\ min}})$. Independent of this detail we find that the corona-based-collection is always several orders of magnitudes faster. For example, to obtain the same Raman signal intensity observed using a 1 second long collection using a corona current of 450 µA (Figure 3-4, condition (c)) requires more than one hour using diffusion-only-transport (current standard, Figure 3-4, condition (d)). The spectral response and noise level of the two experiments (green and black plots) is virtually identical. Identical signal-to-noise level means that the process does not degrade or improve the inherent noise level of the sensor itself, which is what one would expect. Only the response time is improved due to a faster transport of the molecules to the sensor. Identical spectral response also means that the collection process maintains some of the relevant physical properties. The locations of the three major peeks remain consistent with the published values for benzenethiols. [25] Considering the additional results presented in Figure 3-4, we conclude that the solid precipitates previously discussed in Figure 3-3 contain the analyte as well; this was an open point in the discussion before.

3.2.4. Further Enhancements Using the Electrodynamic Lens Based Concentration Concept

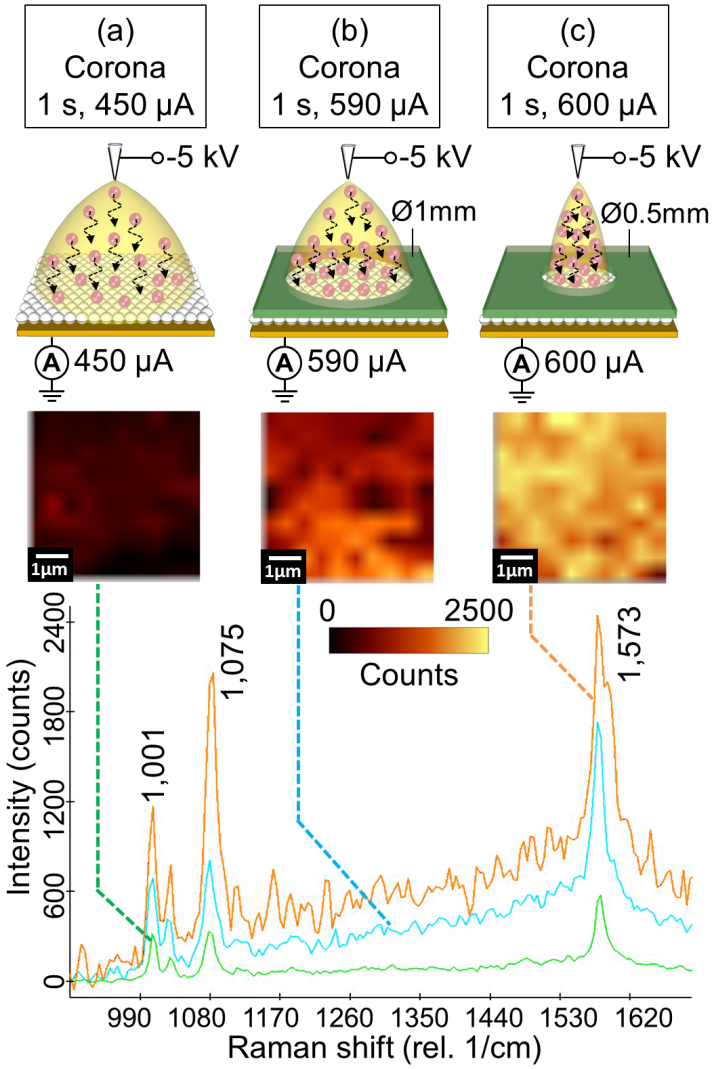

Figure 3-5. Schematics and experimental results comparing different dielectric electrodynamic lens based concentration concepts: (a) corona-based-collection (-5 kV) with 1 second long exposure without a lens (identical to condition (c) in Figure 3-4); (b) corona/lens-based-collection (-5 kV) with 1 second long exposure with a Ø1 mm PDMS lens; (c) corona/lens-based-collection (-5 kV) with 1 second long exposure with a Ø0.5 mm PDMS lens. The corresponding Raman microscopy intensity maps at 1573 cm^{-1} and resulting spectra were recorded in the center of the nanostructured sensor surface in (a) and center of the opening in (b) and (c). Like in Figure 3-4, Raman spectra represent an average recorded by the instrument over a 5µm×5µm sized region. Instrumental settings were identical to the results presented in Figure 3-4 and a relative comparison between the two experiments is possible.

The integration of the nanolens concept on the SERS sensor was found to be more challenging than originally thought. In analogy to Figure 3-2, it requires the integration of a dielectric layer with openings to AgFON surface layer. While we have tested several methods involving standard photolithography it has become evident that the required spin coating, development, and washing steps quench the plasmonic properties of the AgFON thin film we intended to maintain. An alternative working method is presented in **Figure 3-5**, where a 0.5 mm thick PDMS film with an opening of 1 mm (Figure 3-5, condition (b)) and subsequently 0.5 mm (Figure 3-5, condition (c)) was used as the lens forming element. The reason to use PDMS is that it creates a good contact upon placing it onto the SERS layer, it can be removed during optical characterization, it can be reused, and most importantly it will not alter the sensing area; a disadvantage is the relative large size of the lens forming element. Like in the previous experiment (Figure 3-4) the sensor was exposed to 9 ppm of benzenethiol in N_2 for 1 second and the SERS data was recorded using identical recording conditions. Figure 3-5 (bottom) depicts the corresponding Raman microscopy intensity map of benzenethiol at 1573 cm^{-1} band shift and spectra without and with application of the lensing layer. This result extends the size of the lens forming element to the mm-range (the opening sizes presented previously ranged from 200 μm to 1 μm). Despite this difference the results show the same general trend whereby the signal intensity increases from 570 to 1725 and 2445 counts with the introduction and reduction of the opening size. This represents 285, 862, 1222 times the signal recorded using diffusion-only-transport where we recorded 1-2.5 counts (2 was used in the relative comparison) during the same time.

3.3 Conclusion

We generally find that diffusion-only-transport (current standard) is several orders of magnitude slower when compared with the corona/lens-based-collection process. While the experimental results are clear, there are two open questions on the theory when we compare:

(i) the actual charge dissipation rate $J_{current}$ of charged species (corona/lens-based-collection)

$$J_{current} = \frac{I_{corona}}{A_{local}} = \begin{cases} 5.6\times10^{15} e^{-} \cdot cm^{-2} \cdot s^{-1} \; in \; Figure \; 5, condition \; (a) \\ 4.7\times10^{17} e^{-} \cdot cm^{-2} \cdot s^{-1} \; in \; Figure \; 5, condition \; (b) \\ 1.9\times10^{18} e^{-} \cdot cm^{-2} \cdot s^{-1} \; in \; Figure \; 5, condition \; (c) \end{cases} \quad (2)$$

(ii) with the impingement rate R_i of neutral analyte molecules based on Equation 1 (diffusion-only-transport)

$$R_{i,diffusion} = \frac{8.3\cdot10^{22}\cdot P_i}{\sqrt{T\cdot M}} \xrightarrow[300K,\ 110.19 g/mol]{9\ ppm = 0.9\ Pa} 1.3\times10^{18}\ cm^{-2} \cdot s^{-1} \quad (3)$$

First, looking at the actual collection rate using Equation 2 and the SERS signal in Figure 3-5 we noticed that the SERS signal is not directly proportional to the amount of analyte adsorbed on the surface. For example, the opening in condition (c) collects roughly 339 times more material locally than the SERS sensor without lensing structure in condition (a). Yet the signal increases only by a factor of 5. At the same time, we believe that Equation 2 is correct since previous discussed AFM measurements found that the material concentration factor is roughly inversely proportional to the opening area (Figure 3-3). The only explanation as to why the signal increased by only a factor of 5 is that the SERS signal is already saturated due to excessive analyte coverage. It is known that the EM fields associated with the excitation of plasma oscillations decays within a few molecular distances from the surface [39] which explains the observed non-linear response. In the overall theme of things this is perhaps a small detail considering that the signal counts increased by 3 orders of magnitudes when compared to diffusion-only-transport. Second, it is interesting to compare the calculated impingement rate of neutral analyte molecules (diffusion-only-transport) in Equation 3 with the charge dissipation rate of charged species (corona/lens-based-transport) in Equation 2. Doing so we find that the impingement rate is larger than the charge dissipation rate in condition (a) and (b) or on the same order as in condition (c). At first one would anticipate that this cannot be correct. However, it is an important reminder since it points out that the impingement rate is not equal to the rate of analyte adsorption; instead a sticking coefficient smaller than 1 needs to be considered. Many molecules including organothiols reacting with a noble metal surfaces suffer from a low sticking probability. [40, 41] For example, the benzenethiol initial sticking coefficient is calculated to be 1.50×10^{-5}; the detailed derivation can be found elsewhere. [26] So

considering diffusion-only-transport mechanism the rate of molecular adsorption is approximately 10^{13} $cm^{-2} \cdot s^{-1}$, which is sufficiently smaller than the rate of charge dissipation which was on the order of 10^{15} $cm^{-2} \cdot s^{-1}$ without lens, and 10^{17} $cm^{-2} \cdot s^{-1}$ with a single 1 mm in diameter lens, and 10^{18} $cm^{-2} \cdot s^{-1}$ with a single 0.5 mm in diameter lens. We should also point out that the rate of charge dissipation is not equal to the rate of analyte uptake in the corona/lens-based-collection case; there should also be a sticking coefficient in this case. In any event the introduced corona/lens-based-collection mechanism leads to a much faster analyte collection rates which means that the sticking coefficient in this case has to be larger than diffusion-only-transport value of 1.50×10^{-5}.

Based on the current results the introduced corona/lens-based-collection approach increases the amount of locally collected material by at least 3 orders of magnitude. While this appears an incredibly large number we think that this is a conservative estimate. For example, in terms of increased signal intensity the corona/lens-based-collection method led to a 3 orders of magnitude higher signal when compared to the diffusion-only-transport. Considering that the SERS signal saturates under excessive material coverage the intensity measurement would suggest that the actually collected material exceeds the 3 orders of magnitude estimate. For example, if we go back to the AFM height measurement where we used 1 μm sized lens arrays on a 4 μm pitch, the deposits were 257 monolayers tall and formed within 1 second. If we compare this height and time with a diffusion-only-transport case where it takes at least 1 minute for a monolayer to form (using a molecular absorption rate of 10^{13} $cm^{-2} \cdot s^{-1}$ identical to previously published values and a monolayer packing density of ~6.8×10^{14} cm^{-2} on flat Ag [26]) we receive a 4 orders of magnitude faster transport. The previously used wording of "at least three orders of magnitudes" reflects this knowledge.

In conclusion, various nanostructured sensors currently aim for or claim single molecular detection by a reduction of the active sensor size. An equally important challenge, however, can be found in the question "whether the analyte will find the nanoscopic sensing sites". The reduction in the size will ultimately require research on methods which enable localized analyte delivery. The reported corona/lens-based-collection concept is a first step in this direction. The approach is not limited to the SERS

sensor or analytes that we have tested in this study and should provide equal improvements in terms of response time in other sensor designs. Others adapting this concept should anticipate at least 3 orders of magnitude improvement in response time over system that use diffusion-only-transport. Moreover, the ultimate level of improvement is not yet known. This would require testing of a wider range of opening sizes and pitch distances in terms of the lens design. It would also be beneficial to test a wider range of analyte molecules with poor or high sticking coefficients. We also see a potential for the introduction of an active matrix type analyte collection system that collects analytes at various points on a substrate at different times. The minimal 1 second long exposure time is presently a practical limitation and not representative of the minimal exposure time that is required to identify the various analytes and concentrations we tested in this study.

3.4 Experimental Section

Aerosol Preparation: Various types of aerosols were used in this study. Specifically, we tested gas mixtures (aerosols) containing large microscopic particles Kentucky blue grass pollen (Sigma-Aldrich®), fluorescent CdSe nanoparticles (Lumidot™), all the way down to small molecules such as fluorescent Alq_3 (Sigma-Aldrich®), fluorescent anthracene (Sigma-Aldrich®), non-fluorescent tobacco smoke (nicotine, tar, *etc.*), and non-fluorescent benzenethiol (Sigma-Aldrich®). The corresponding aerosol preparation methods are: (i) Pollen (a loose powder) was carried into the collection chamber using 2000 sccm N_2 flow. It is used to show collection ability of an allergenic substance. (ii) Alq_3/CdSe quantum dots containing aerosol was generated using atomization. Specifically, Alq_3 (5 mg) was first dissolved in tetrahydrofuran (THF, 1 mL) solution. The solution was then dropped on an atomizer (an ultrasonic vibrating mesh) at a constant rate. The atomization rate was approximately 0.01 $mL \cdot s^{-1}$. The aerosol was further diluted with 2000 sccm N_2 which also serves as a carrier gas to transport the analyte into the collection chamber. The calculated concentration (using 459.43 Dalton) was ~73 ppm. The aerosol containing CdSe quantum dots were prepared using the same method. Here a CdSe quantum dots solution (5 mg/mL in toluene) were used. The atomization rate was approximately 0.01 $mL \cdot s^{-1}$ which was further diluted with 2000 sccm N_2. The calculated concentration (using 1.4×10^5 Dalton) was ~238 ppb (parts per billion). (iii) Anthracene containing aerosol was generated

by thermal evaporation. Anthracene is a white solid in powder form with a melting point of 210-215 °C. In this experiment, anthracene was thermal evaporated at 250 ºC. The evaporation rate was estimated to be 0.2 $mg \cdot s^{-1}$ by measuring the weight reduction in certain amount of time. The carrier gas was 2000 sccm N_2. The calculated concentration (using 178.23 Dalton) was ~750 ppm. (iv) Tobacco smoke containing aerosol was generated using smoldering. A cigarette was smoldered at a constant rate using 10 sccm air. The smoke was then diluted using 2000 sccm N_2. We have not further analyzed the composition of the aerosol which is known to contain more than 2000 chemicals. A primary constituent is tar and nicotine which are soft solid and liquid like substances at room temperature. (v) Benzenethiol containing aerosol was generated using a bubbler based evaporation. Specifically, the benzenethiol was introduced using a conventional bubbler approach with a flow rate of 10 sccm N_2 in the bubbler line. The vapor pressure of benzenethiol is 1.4 mmHg at room temperature which is equivalent of 1800 ppm of benzenethiol molecules inside the bubbler and 9 ppm after dilution with 2000 sccm N_2.

AgFON Substrate Fabrication: Silicon wafers were first put in HF solution for 30 seconds to remove native oxide. After cleaned by acetone, methanol, IPA and rinsed by DI water, the wafers were treated in piranha etch at 120 ºC for 30 minutes, and then in 5:1:1 ratio of H_2O:NH_4OH:H_2O_2 for 30 minutes to make the surface hydrophilic. Surfactant-free, silica nanosphere suspensions (Bangs Laboratories, Inc., 200 nm, 4 wt%) was further diluted in ethanol (1:1 volume ratio), which served as a spreading agent. The suspension was dropped onto a water surface which yields a surface layer of silica beads. The Langmuir-Blodgett method was used to compact the beads and to transfer the beads to the target wafer. After drying the surface for 30 minutes, the AgFON standard substrate was completed through e-beam evaporation of 20 nm/180 nm Cr/Ag films to form the plasmonic cap layer.

PDMS Lens Fabrication: 184 silicone elastomer base (Sylgard®, 20 g) and 184 silicone elastomer curing agent (Sylgard®, 2 g) were well mixed in a plastic cup. The cup was then placed in a desiccator to degas for 30 minutes. The mixture was then slowly poured into a petri dish followed by another 30 minute degas process. The amount of the mixture was controlled so that the thickness of the film was kept 0.5 mm. The PDMS was

then cured in an oven at 70°C for an hour. After curing, the film was cut into 5 mm wide and 10 mm long pieces. The lens was made on PDMS film by a 1 mm or 0.5 mm hole punch.

SERS Characterization: SERS spectra and corresponding Raman microscopy intensity maps were acquired using a confocal Raman microscope system (Witec Alpha 300R) equipped with an objective lens (Nikon 100×, 0.90 NA in air). A 514 nm argon ion laser was used as a laser source, which was set to a constant power of ~2 mW for all SERS measurements in this report. The scattered light was analyzed using a 600 mm^{-1} spectrometer grating with a spectral resolution of about 3 cm^{-1}. The collection area was defined by a 5μm×5μm region with a 10×10 sampling density. The collection time for each sampling spot was 1 second. The reflectance absorption spectrum was analyzed using a VIS-NIR spectrophotometer (Ocean Optics, USB4000 VIS-NIR spectrometer, QR400-7-UV–vis reflection probe). The reflectance absorption spectrum of AgFON was collected and used for the chosen wavelength (514.5 nm).

Chapter IV

Active Matrix Based Collection of Airborne Analytes: An Analyte Recording Chip Providing Exposure History and Finger Print

Jun Fang, Se-Chul Park, Leslie Schlag, Thomas Stauden, Jörg Pezoldt, and Heiko O. Jacobs

***Adv. Mater. 26**, 7600 (2014).*

1. Introduction

The desire to detect and identify trace amounts of airborne analytes, including combustible or toxic gases, small molecules, particles, viruses or bacteria with ever increasing sensitivity and selectivity continues to be one of the main drivers in sensor research and analytical science. [20, 21, 42] A common approach in recent years has been to integrate the required analytical components into a small form factor to allow "onsite" detection at low cost. However, there are many cases where complexity and physical laws prevent scaling to small dimensions. For example, recognition by morphology still requires analyte specific forms of microscopy. [14, 43] Equally, recognition by electromagnetic properties requires appropriate spectroscopic methods. [44, 45] Independent of the specific situation, these techniques are relatively complex and are often performed at centralized "offsite" facilities. In all cases, it is usually required that the analyte is collected on the surface of a sensor (for onsite detection) or substrate (for offsite detection), which brings up the question of how to transport an airborne analyte to the target surface. The collection is often based on diffusion-only-transport whereby the analyte reaches the substrate on a random walk at a low rate. [11-13, 22, 23]

Different from this practice, this communication discusses ideas and first experimental results towards an active matrix based analyte collection approach referred to as "Airborne Analyte Memory Chip/Recorder", which (i) takes samples of the particles or molecules in an aerosol at specific points in time, (ii) transports the analyte sample to a designated spot on a surface, (iii) concentrates the analyte at this spot to achieve an amplification, (iv) repeats this sequence until the recording matrix is full, and (v) reads out the analyte matrix on the chip. The approach discussed here uses a directed force to transport and concentrate analytes at predetermined points on a surface at a rate which exceeds non-directed diffusion-only-transport by several orders of magnitude. The approach has recently become relevant considering a trend in sensor designs, which has focused on the reduction of the active sensor size to increase the sensitivity to a point where it is possible to detect single binding events. [15, 24, 27, 28] At present most reports used diffusion-only-transport as a method, by which the analyte is transported to the sensing elements. Considering the fact that the sensing element is shrunk down to point like structures, diffusion-only-

transport is not the best approach. Specifically, basic gas laws show that the number of analyte particles impinging on a surface goes to zero for point like structures. In other words, it becomes increasingly unlikely for an analyte molecule at low concentrations to "find" and interact with an ever increasingly small sensor, trading the gained sensitivity with a slow response time. The solution to this problem is to use a directed force to transport the analyte from a distance away to predetermined sensing points at a higher rate, which has recently been discussed elsewhere. [5, 6, 24] This communication adds the ability to collect and store analytes in an active matrix array like fashion, at predetermined points on a surface, at different points in times. As a consequence, the technique is able to provides a time record or memory of the events that occurred in the past yielding an average exposure, peak exposure, and exposure of various species on an as needed basis.

The approach is inspired by developed transport strategies in the aerosol community to collect airborne particles using convection, [29] thermophoretic, [30] magnetic, [31] and Coulomb [4, 35] forces. The use of Coulomb forces has been chosen since localized collection of organic [18] and inorganic nanoparticles [5, 6, 8, 9] has already been demonstrate with an unmatched sub 100 nm lateral resolution. While some sensors based on electrostatic precipitators are known, [5, 6, 24, 45] an active matrix type analyte collection chip has not yet been demonstrated. This communication reports the collection of analytes over a wide range of molecular weights including (i) microscopic particles (Kentucky blue grass pollen, 20 μm in diameter, ~3×10^{17} Da), (ii) inorganic nanoparticles (Cu nanoparticles, 40-60 nm in diameter, ~3.5×10^{8} Da; CdSeS/ZnS nanoparticles, 6 nm in diameter, ~3.4×10^{5} Da), all the way down to (iii) small organic molecules (MEH-PPV, 1.5×10^{5}-2.5×10^{5} Da; Alq_3, 459.43 Da; anthracene, 178.23 Da; 4-fluorobenzenethiol 128.17 Da; benzenethiol, 110.19 Da). In the currently analyzed cases we find that the collection amount is increased by several orders of magnitudes comparing to the case where collection is driven by diffusion-only-transport. In addition to conventional microscopic analytical techniques, and to provide a quantitative analysis, we demonstrate that the collection scheme is compatible with more sophisticated analytical concepts, and specifically with surface-enhanced Raman spectroscopy (SERS) to provide a signature and finger print of adsorbed molecular layers.

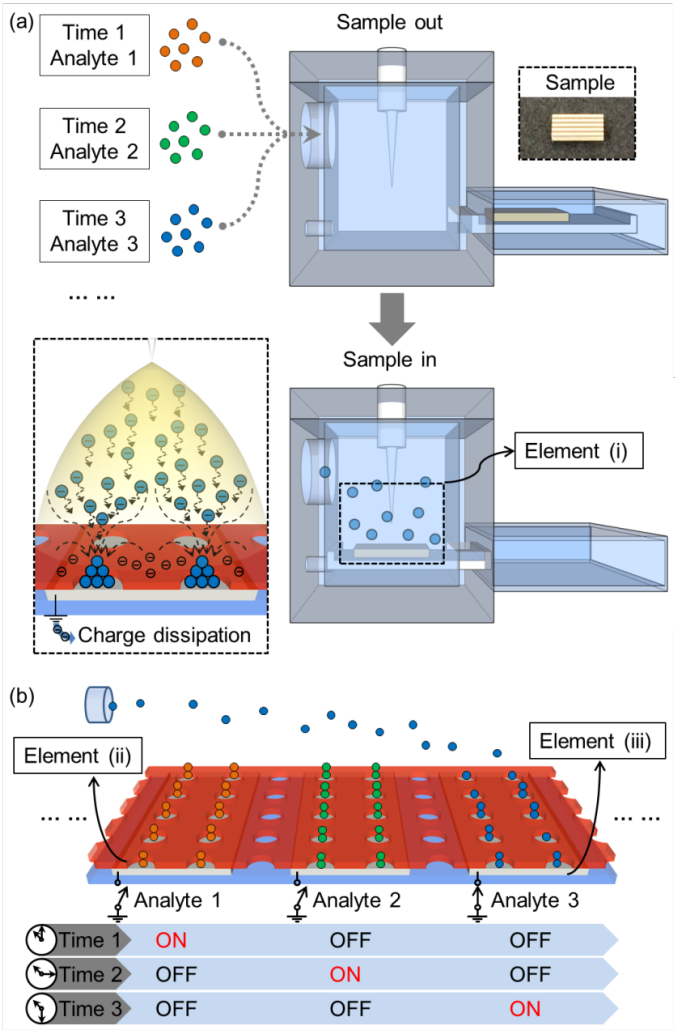

Figure 4-1. Schematic of experimental recording platform to collect analytes in an aerosols at a known concentrations and different times using an "Analyte Memory Chip/Recorder" incorporating three design elements: (i) a Corona discharge based analyte charging method, (ii) an electrodynamic lens based analyte concentration concept (red insulating negatively charged film with openings), and (iii) an electrically biased domain electrodes based active matrix design (grey electrodes underneath the red film).

Figure 4-1 describes the experimental testing platform and the realized "Analyte Memory Chip/Recorder" that is used to test aerosols containing a variety of analytes at a known concentration. The "Analyte Memory Chip/Recorder" incorporates three design elements: (i) a Corona discharge based analyte charging method, (ii) an electrodynamic lens based analyte concentration concept, and (iii) an electrically biased domain electrodes based

active matrix design to enable analyte collection and storage in selected recording sites at selected times. All analyte collection experiments use the collection chamber depicted in Figure 4-1(a) which was machined out of an insulating acrylic block to provide a 3cm×3cm×3cm cavity, a 10 mm in diameter gas inlet, a 3 mm gas outlet, a pointed copper electrode 5 mm above the sample, a sample port and a sample tray. At 5 mm, a Corona discharge can be generated using a 12V-5kV solid state high voltage converter (Gamma High Voltage Research, Inc., MC50). At a much shorter distance, a high current breakdown occurs which damages the substrate. Equally, at a much larger distance, we were not always able to get a stable Corona discharge using this converter. The sample tray was designed so that it can be shifted back and forth between two sealed positions. This design maintains the constant concentration of analytes in the chamber and enables a short exposure time. Analytes from various origins (discussed later) are introduced to the collecting chamber at different times. The Corona discharge occurs only as the sample (with a grounded domain electrode) is shifted to the exposure position which is underneath the negatively biased pointed electrode. Details of the Corona discharge based analyte charging method have been published previously. [5] In short, positive ionization occurs within a fairly thin ionizing plasma region (not shown), [36] where the electric field is sufficiently strong to cause the emission of electrons through the photoelectric effect which subsequently produce positive gaseous species and secondary electrons through impact ionization. [37] Beyond this region (shown), electrons with energy lower than ionization energy will attach to neutral analytes yielding negatively charged analyte particles. These negatively charged species move downwards until they reach the grounded collection electrode. When compared to conventional point to conducting plate Corona discharge experiments, [47] this report adds a patterned dielectric thin film with openings to the conductive plate to form a single or arrays of lensing structures. The purpose of the introduced dielectric lensing structures is to provide an electrodynamic funnel to transport the analyte from a distance away to desired collection points. The function of this design element has been reported previously. [5] In brief, the dielectric lensing structure is negatively charged through the deposition of electrons, which in turn produces the depicted fringing field. In our case, this design element is used to divert the charged analytes to the desired points and to increase the flux and concentration of adsorbed materials in small points leading to an

amplification of the analyte. Figure 4-1(b) incorporates all three design elements, adding "the externally biased domain electrodes" to the conceptual approach to achieve an active matrix like collection system. The domain electrodes that are left floating represent the OFF position (charge dissipation disabled); charge dissipation and steady state collection of analyte is blocked on floating electrodes. On the other hand, the domain electrode connected to ground represents the ON position (charge dissipation enabled). Collection of the analytes occurs on these domain electrodes at a level that is several orders of magnitude higher (discussed later) than in regions that are not electrically connected. The advantage of keeping regions floating and others connected to ground is that it leads to a self-equilibrating potential profile, whereby the transporting field of the charged analyte points to the grounded collection sites. Locally the field cannot point towards floating regions. If it would, the potential profile would adjust since no charge dissipation is possible on floating domains on a steady state basis.

2. Results

Figure 4-2 provides results of a first set of experiments testing the "Corona/lens-based-collection" (design elements 1 and 2) concept to demonstrate that the process is generally applicable independent of the analyte type. The use of more than one domain electrode (active matrix, design element 3) will be discussed later. In the particular set of experiments a periodic electrodynamic lens array is used. The lens array is defined using a patterned 500 nm thick layer of insulating photoresist (s1805, Microposit™) with 200 μm square (Figure 4-2(a)) or 1 μm circular (Figure 4-2(b-h)) openings to a flat silicon substrate which forms a single equipotential domain. All chips were 5 mm wide and 10 mm long.

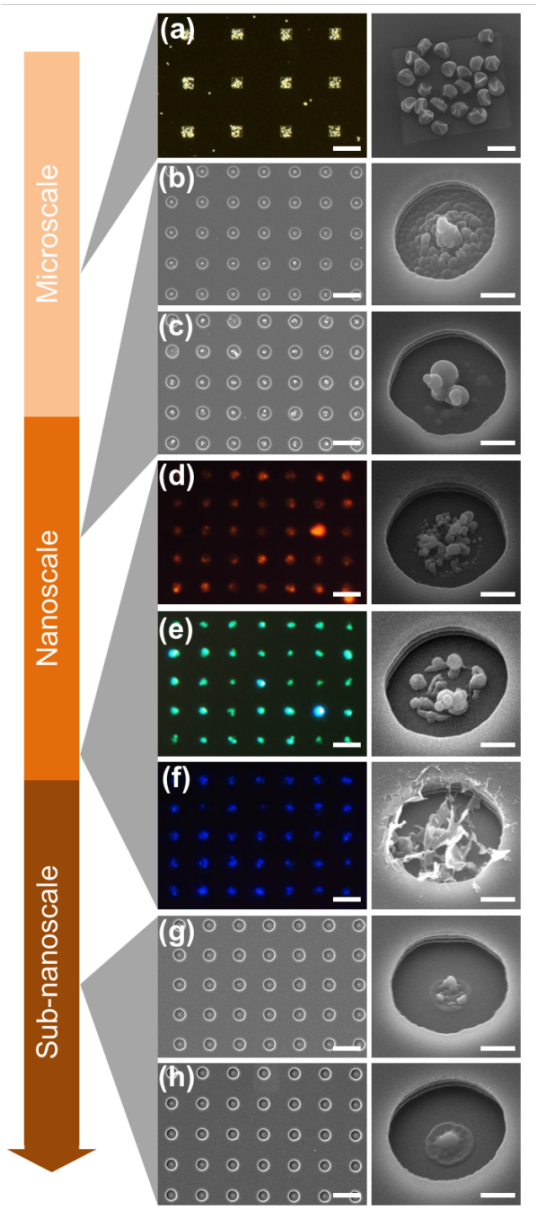

Figure 4-2. *Micrographs of Corona/lens-based-collection of various analytes representing a wide range of molecular weights (from 3×10^{17} to 1×10^{2} Da). (a) Optical microscope image of locally collected Kentucky blue grass pollen. (b-c) SEM images of locally collected Cu nanoparticles and CdSeS/ZnS nanoparticles. (d-f) Fluorescent microscope images of locally collected MEH-PPV, Alq_3 and anthracene. (g-h) SEM images of locally collected 4-fluorobenzenethiol and benzenethiol. SEM closeups for each analyte are shown on the right. The scale bars are 500 µm in (a, left), 50 µm in (a, right), 5 µm in (b-h, left) and 500 nm in (b-h, right).*

Table 4-1. *List of the analytes, their concentrations, weights, and sizes.*

Analyte	Concentration	Weight	Size
Pollen	Unknown	~3×10^{17} Da	~20 μm
Cu nanoparticles	<1 ppb	~3.5×10^{8} Da	~40-60 nm
CdSeS/ZnS nanoparticles	~99 ppb	~3.4×10^{5} Da	~6 nm
MEH-PPV	~168 ppb	1.5×10^{5}-2.5×10^{5} Da	~5 nm
Alq_3	~73 ppm	459.43 Da	~2 nm
Anthracene	~750 ppm	178.23 Da	~1 nm
4-FBT	~19 ppm	128.17 Da	~3 Å
BT	~9 ppm	110.19 Da	~3 Å

In the experiments we tested a wide spectrum of aerosols. **Table 4-1** provides a list of the analytes, their concentrations, weights, and sizes. The goal was to test and demonstrate collection of analytes over the largest possible range of molecular weights to illustrate the generality of the approach. As a consequence several different aerosol preparation methods had to be used. In short (i) atomization of a liquid containing suspended solid or dissolved analytes was used in the case of Cu nanoparticles, CdSeS/ZnS nanoparticles, MEH-PPV, and Alq_3; (ii) direct thermal evaporation of a solid analyte was used in the case of anthracene; and (iii) evaporation of a liquid analyte inside a bubbler was used in the case of 4-fluorobenzenethiol (4-FBT) and benzenethiol (BT). All analytes were introduced to the testing chamber using 2000 sccm of N_2 as a carrier gas. A negative Corona discharge (-5kV) was applied between the tip and the chips during a 1 second exposure time. The optical/fluorescent micrographs and SEMs illustrate the range of analyte particles that can be collected depicting Kentucky blue grass pollen (Figure 4-2(a)), Cu (Figure 4-2(b)) and CdSeS/ZnS (Figure 4-2(c)) nanoparticles, all the way down to small molecules such as MEH-PPV (Figure 4-2(d)), Alq_3 (Figure 4-2(e)), anthracene (Figure 4-2(f)), 4-FBT (Figure 4-2(g)) and BT (Figure 4-2(h)).

From an experimental point of view the following general results and observation are important: First, independent of analyte type or size, it is possible to transport, concentrate,

and collect the various analytes at predetermined sensing points using the introduced Corona/lens-based-collection process, which is remarkable considering the large range of analytes we tested. In terms of molecular weight the results represent a range of 3×10^{17} to 1×10^{2} Da. Second, the structures and at least some of the relevant physical properties remain intact. For example: (i) shape of the pollen particles; (ii) element composition of Cu and CdSeS/ZnS nanoparticles; (iii) fluorescent characteristics of the MEH-PPV, Alq_3 and anthracene molecules; and (iv) spectral response due to Raman scattering (discussed later) of BT and 4-FBT, remain intact. Third, the localized collection rate is large comparing to commonly used approach where the analytes deposit randomly on the surface by diffusion-only-transport. In the case of BT and 4-FBT (quantitative measures will be provided later), the collection rate was determined to be 3 orders of magnitude faster than diffusion-only-transport. This is remarkable since it means that it should be possible to achieve an electrically driven collection/storage approach of analytes in addressable points without having a high level of cross contamination due to the diffusion-only-transport. The gained knowledge leads to the following active matrix idea using biased domain electrodes.

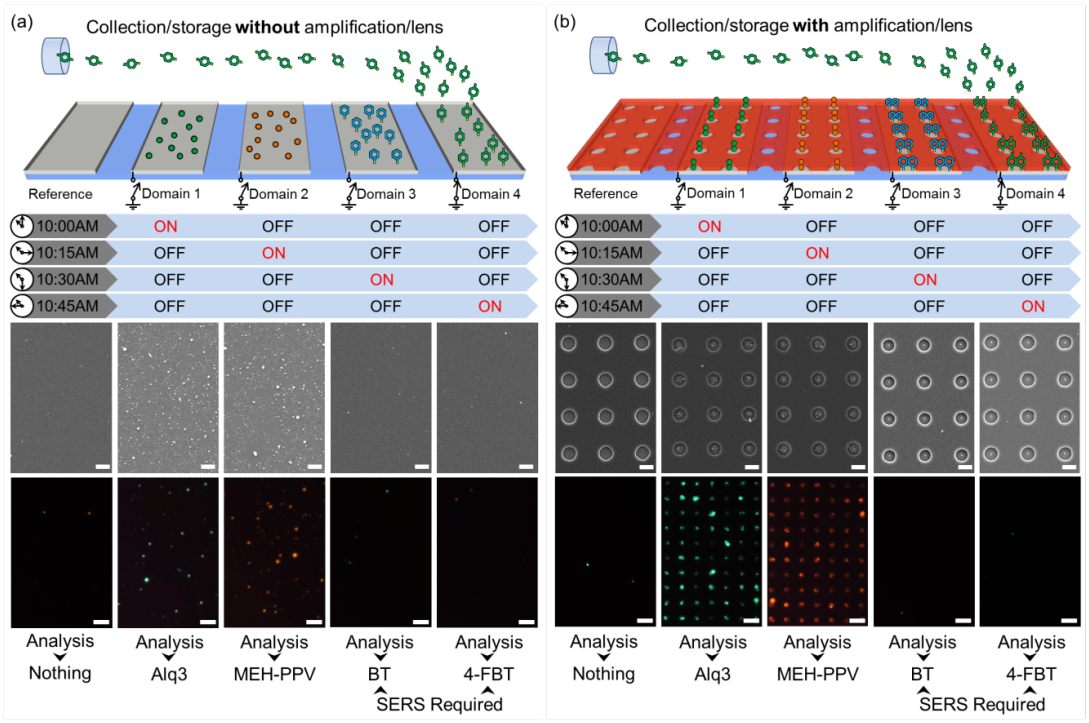

Figure 4-3. *Active matrix based analyte collection/storage using externally biased domain electrodes (a) without and (b) with localized lens based concentration/amplification. Each*

domain represents a memory cell which collects analyte at a specific point in time through the application of electrical ground leading to a time record of past events. SEM and fluorescent microscope images of locally collected Alq_3, MEH-PPV, BT and 4-FBT are shown as first set of analytical tools to read out past events. The introduced lens leads to an amplification/increase of the analyte concentration in predetermined spots which aids in the detection. The scale bars are 1 μm for SEM images and 5 μm for microscope images.

Figure 4-3 provides a set of results which combines and compares all design elements of the active matrix based analyte collection/storage chip. This set of experiments uses the introduced domain electrodes to control the material flux spatially in an active matrix array like fashion. The images in Figure 4-3(a) use domain electrodes without dielectric lensing structures while the images in Figure 4-3(b) represent the results where a dielectric lensing structure is added to increase the analyte concentration locally. The conceptual drawing is shown next to the results. In all cases, domain electrodes (gray region) that are left floating represent the OFF position (charge dissipation disabled). On the other hand, the domain electrode connected to ground represents the ON position (charge dissipation enabled). Experimentally the concept is tested using an insulating sapphire chip that provides a support to electrically isolated electrodes fabricated by standard photolithography. The size of the chips was 5mm×10mm carrying 0.5 mm wide Ag strips with a 0.5 mm gap. Each chip had 5 electrically separated collecting domains. Again the illustrated 1 μm in diameter dielectric lensing structures (red layer) act as funnels for the analyte to be concentrated in predetermined points. The layer is identical to the one used in the description in Figure 4-2.

Samples of the aerosols in the test chamber were taken at different times. The test chamber contained Alq_3 at time 1 (10:00 AM), MEH-PPV at time 2 (10:15AM), BT at time 3 (10:30AM), and 4-FBT at time 4 (10:45AM). The sampling time was 1 second in all cases under a -5kV negative Corona discharge. Generally, we find that there is little crosstalk between the individual domains which means that diffusion-only-transport is much slower that the Corona based analyte transport onto the biased domains. For example, the electrically floating reference domain (far left) does not show detectable amounts of

precipitates on the surface which means that diffusion-only-transport is much slower than directed Corona-based-transport.

Out of the four analytes, two had a fluorescent signature Alq_3 (domain 1, green) and MEH-PPV (domain 2, red) and the location of the fluorescence confirms the storage of the analyte at the correct site. Domain 3 and 4 were used to collect BT and 4-FBT molecules which are very small molecules without any fluorescent properties. As anticipated no detectable amount of fluorescence is visible in these domains, which means that cross contamination through diffusion-only-transport from the surrounding domains can be neglected. Comparing the images in Figure 4-3(a) with the images in Figure 4-3(b) provides a qualitative measure of the analyte amplification factor that can be gained introducing the lensing structures. Each lens funnels the flux of analyte to a specific collection point, forming an array of analyte hotspots that help detection. The SEM images in domain 3 and 4 show small amounts of precipitates inside of the center of each lens. Again the Alq_3 and MEH-PPV were fairly straight forward substances that simplified the detection based on fluorescence microcopy. This is not the case considering the BT (domain 3) and 4-FBT (domain 4) containing aerosol. Although the analytical techniques used in Figure 4-3 (b, SEM, lens opening center) suggest that some precipitates are present, an identification is not possible using the presented data. The following section will carry out an experiment which will confirm that the visible precipitates contain the target molecules. The experiment uses surface enhanced Raman spectroscopy (SERS) as an analytical tool.

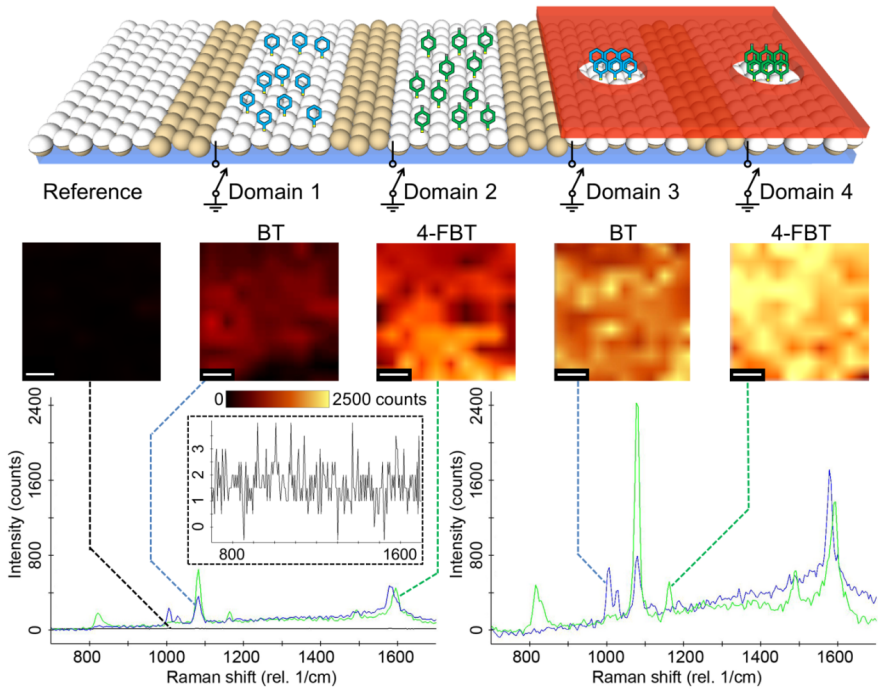

Figure 4-4. *Recording elements integrated on SERS sensor, illustrating schematics (top), next to corresponding Raman microscopy intensity maps at 1075 cm^{-1} (middle), and resulting spectra (bottom). BT analyte is collected on domain 1 and 3, and 4-FBT is collected on domain 2 and 4. On domain 3 and 4, a 0.5 mm thick PDMS mask with a 0.2 mm opening is used as an electrodynamic lens to achieve an amplified analyte collection. Raman intensity maps show raw unprocessed data recorded at 1075 cm^{-1} using the same microscope settings. Raman spectra represent an average recorded by the instrument over a 5µm×5µm sized region. An offset (up down) correction has been applied for the spectra to overlap at the beginning of the graph. Peak height measurement and relative comparison is not effected. The scale bars are 1 µm.*

This section demonstrates and quantifies how this general strategy improves the collection efficiency of an existing SERS sensor design. Specifically, we integrated the collection scheme on an existing SERS sensor that is sensitive to the adsorption of small molecules such as BT and 4-FBT discussed previously. **Figure 4-4** provides a schematic of the designs we tested. Instead of using a simple Ag strip, the particular SERS sensor requires the use of an AgFON enhancing layer, which stands for a "standard" in the field of SERS detection. [48] In brief, the AgFON enhancing layer is a closely packed self-

assembled layer of 150 nm in diameter silica nanospheres, where the top half is coated with 20 nm/180 nm Cr/Ag. In addition, we introduce lensing structures (design element 2) and biased domains (design element 3) in the schematic (Figure 4-4, top). The white regions are conducting Ag coated silica nanospheres which are surrounded by uncoated insulating regions. The white conductive regions represent the domain electrodes to control the collection/storage of analytes using the Corona-based-transport. On domain 3 and 4, a 0.5 mm thick PDMS film (shown in red) with an opening of 0.2 mm is used as the lens forming element. The reason to use PDMS is that it creates a good contact upon placing it onto the SERS layer, it can be removed during optical characterization, it can be reused, and most importantly it will not alter the sensing area. The same aerosol containing analytes as previously described were used. Specifically, BT (9 ppm) and 4-FBT (19 ppm) molecules are charged using a negative Corona discharge (-5 kV).

During the collection process, domain 1, 2, 3 and 4 are turned on (grounded) sequentially to store whatever analyte is present in the aerosol at the respective time at predetermined storage sites. Only one electrode is grounded each time for about 1 second and the others are left floating. The placement of the substrate is slightly shifted each time so that the tip is vertically above the grounded domain. We always took the region that is in the center of the strips for a relative comparison since there is a drop in the concentration within the edge region of the strips. The tapered region is fairly narrow typically less than 1 mm wide. The molecules were recorded using Raman microscopy three days later which means that the information can be retained for a sufficiently long time. All Raman microscopy intensity maps (Figure 4-4, middle) and resulting spectra (Figure 4-4, bottom) were recorded under identical exposure and recording conditions to provide a relative comparison of the various design elements. The results are interesting: First, the reference domain shows again no detectable signal and a much longer (0.5 to 1 hour) exposure time is required to detect signatures of the target molecules on floating "diffusion-only-transport-domains". This agrees with previous result and means that diffusion-only-transport is not fast enough to cause a detectable signal in 1 second. Second, on domain 1 and 2, a dramatic increase in the signal (350 and 639 counts at 1075 cm^{-1}, respectively) is observed. This again agrees with previous results and means that introduced Corona based transport in combination with biased domains is highly efficient in the collection of all

kinds of particles all the way down to molecular sized species. The location of the peeks of Raman spectra remain consistent with published values for BT and 4-FBT, [25] indicating the relevant physical properties remain intact. Third, the introduction of the electrodynamic lens based design elements on domain 3 and 4 leads to an additional amplification (increased to 831 and 2456 counts at 1075 cm^{-1}, respectively) due a localized increase in the amount of analyte that is collected. This is interesting since the diameter of lens opening is a factor of 200 times larger than what was used in Figure 4-3 which means that the lensing effect is not limited to a predetermined opening of only one diameter.

To provide a relative comparison of the effectiveness of the various design elements we made an attempt to provide a first order estimate by comparing the signal intensity recorded at 1075 cm^{-1} on the 5 different domains. Since the diffusion-only-transport-domain (reference domain) is not showing a detectable amount of material, a relative comparison would lead to large errors. To prevent this, we ran additional experiments with a 10 second long exposure and were able to record 8 counts for BT and 15 counts for 4-FBT on electrically floating diffusion-only-transport-domains. The extrapolation provides a base level of 0.8 counts for BT and 1.5 counts for 4-FBT considering a 1 second long exposure. In terms of a relative comparison, the design elements "(i) Corona discharge based analyte charging method" in combination with the "(iii) electrically biased domain electrodes" increases the collection of the analytes by at least a factor of 400 (specifically, 437 and 426 in domain 1 and 2, respectively) when compared to the standard diffusion-only-transport approach. This number can further be increased to a factor exceeding 1000 (specifically, 1038 and 1637 in domain 3 and 4) through the introduction of the design element "(ii) electrodynamic lens", which provide a localized amplification of the analyte on the biased domain electrodes. In other words, the introduced collection and amplification process are highly effective to collect and locally store analyte at predetermined points. The recorded signals are 2 to 3 orders of magnitude higher when compared with the standard diffusion-only-transport approach. While this appears to be a very large number we think that this is a conservative estimate in terms of amount of material that is collected. Considering that the Raman signal saturates under excessive material coverage the intensity measurement would suggest that the actually collected material exceeds these estimates. [39] Moreover, it should be possible to increase the

values further through optimization of the opening size, pitch, domain size and domain potential. For example, a smaller pitch and higher potential should allow a further increase in the amount of material that can be collected locally compared with the standard diffusion-only-transport approach.

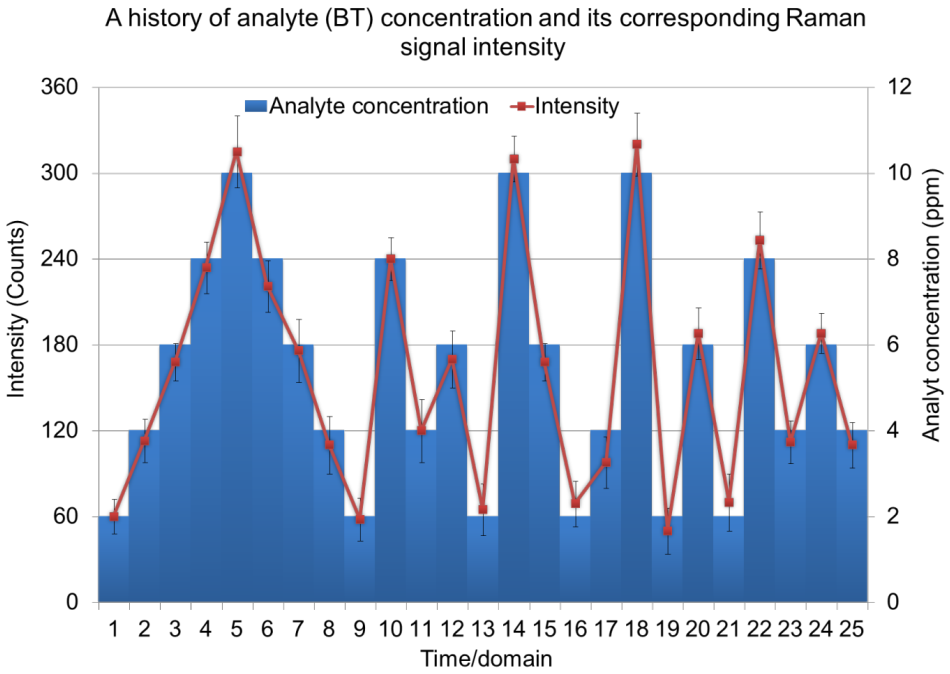

Figure 4-5. *Recovered BT analyte concentration measured as Raman counts (red line, Raman signal intensity at 1075 cm^{-1}) analyzing 25 recording sites. The actual analyte exposure concentration (blue bars, in ppm) is used as a background to help in the comparison. In the experiment, 25 sequentially grounded domain electrodes were used to record the concentration of BT over a period of 12 hours using a 1 second long sampling time every 30 minutes. The concentration of BT was randomly changed every 30 minutes to be 2 ppm, 4 ppm, 6 ppm, 8 ppm or 10 ppm (blue bars). The recovered signal intensity (red line) agrees well with the actual concentration.*

Figure 4-5 provides a result where the introduced analyte recording chip is used to retrieve past/historical analyte concentration. Samples of the environment were collected in 30 minutes intervals providing a time record over a 12 hour period. Specifically, the analyte (BT) concentration was randomly set to be 2 ppm, 4 ppm, 6 ppm, 8 ppm or 10 ppm during the collection cycle. The collection process is identical as previously described.

After the collection, the offsite SERS data taken from the various domains again allow an identification of the BT. For each domain/time, the Raman signal intensity at 1075 cm^{-1} is recorded (red line). We repeated the experiment over a period of three days using the same analyte sequence and the plot indicates the mean value and deviation (STD). The actual analyte concentration of the aerosol is shown as well to provide a comparison (blue bars). The comparison shows that it is possible to retrieve the information of prior exposure concentrations. We have not yet established the ultimate limits of how many recording sites can be integrated. The number 25 is currently only limited by the number of electrical connections that we can make and handle. The experiment in Figure 4-5 used five chips whereby each chip had five electrically separated domains.

3. Conclusions

The application of the discovered process as an active matrix analyte recording chip has been limited by the number of electrical connections that we can make. From a practical point of view, a multiplexing concept would have to be introduced to further increase the number of isolated recording sites. From a physical point of view, however, it should be possible to achieve a larger number of recording sites than what has been demonstrated. The spatial resolution (spot size was 1 μm in Figure 4-3 and 200 μm in Figure 4-4) suggest that a much higher integration density can be attained. However, crosstalk rather than integration density, is likely going to be the limiting factor. Specifically, the analyte transport based on random diffusion was 400 to 1000 times slower than the directed transport method used in this study. This means that it should be possible to record a sequence of 400 to 1000 analyte exposures before diffusion based cross-contamination becomes the limiting factor. The basic idea is that such a chip could be a commodity item that is placed in an environment that a user would like to keep a record from. The information is retrieved on an as needed basis. Offsite analysis of the chip storing the information would make this approach more economical than an online monitoring system for all kinds of threads. The conceptual approach of a simple recording device can be compared to RADON collectors that are placed into millions of households in the US for a period of time to record an integral value of RADON exposure. The recording container is closed and returned to centralized analytical facility, which measures the accumulated

exposure dosage using expensive analytical tools to reduce the cost and maintain a standard. Our approach is different in the sense that it provides a time record.

A second and more immediate application relates to improvements in the response time that can be gained using the directed transport schemes that have been introduced. For example, a 1 second long exposure to BT analyte was sufficient to obtain 350 counts at the characteristic 1075 cm^{-1} peek (Figure 4-4, blue, without lens) which is a short time considering the low analyte concentration (9 ppm) that was used in the experiment. It is not possible to detect such a low analyte concentration using the diffusion-only-transport standard unless a much longer exposure time is used. For example, it took a 1 hour long exposure using diffusion-only-transport to achieve the same signal intensity level. This is perhaps the most important result of this study since this general trend holds true over a very large range of analyte particles (14 orders of magnitude in terms of molecular weight, Figure 4-2). As a consequence, the approach should benefit any sensing concept that involves a surface sensor and not just SERS. What it means is that others adapting this concept should anticipate several orders of magnitude increases in response time over sensing systems that use diffusion-only-transport to the surface sensor they use.

Finally, the ability to direct analytes to nanoscopic sensing points using the nanolens is also relevant in light of recent research on nanosensors, where a trend has been to shrink down the active sensor area to a point to detect single molecular binding events. While this trend increased the sensitivity, it came at the price of a slow response time since it is increasingly unlikely for a molecule to "find" the nanoscopic sensing elements/points using the diffusion-only-transport, as impingement and capture rates scales with the area of the sensing element. As a consequence, the introduced nanolens based transport can be employed to increase the collection speed and localized concentration of the analyte on nanoscopic sensing elements to acceptable levels.

4. Experimental Section

Aerosol Preparation: Various types of aerosols were used in this study. Specifically, we tested gas mixtures (aerosols) containing large microscopic particles Kentucky blue grass pollen, Cu and CdSeS/ZnS nanoparticles, all the way down to small molecules such

as fluorescent MEH-PPV, Alq_3 and anthracene, non-fluorescent 4-fluorobenzenethiol and benzenethiol. All of the materials were purchased from Sigma-Aldrich: (a) Pollen (a loose powder) was carried into the collection chamber using 2000 sccm N_2 flow. It is used to show collection ability of an allergenic substance. (b) Cu and CdSeS/ZnS nanoparticles/MEH-PPV/Alq_3 containing aerosol was generated using atomization. Specifically, the aerosol containing Cu or CdSeS/ZnS nanoparticles were prepared using toluene solution (5 mg/mL). The solution was then dropped on an atomizer (an ultrasonic vibrating mesh) at a constant rate. The atomization rate was approximately 0.01 $mL \cdot s^{-1}$. The aerosol was further diluted with 2000 sccm N_2 which also serves as a carrier gas to transport the analyte into the collection chamber. The calculated concentration (using 3.5×10^8 Da for Cu and 3.4×10^5 Da for CdSeS/ZnS) was <1 ppb for Cu and ~99 ppb for CdSeS/ZnS. Similarly, MEH-PPV and Alq_3 was first dissolved in tetrahydrofuran (THF) solution (5 mg/mL), separately. The atomization rate was approximately 0.01 $mL \cdot s^{-1}$ which was further diluted with 2000 sccm N_2. The calculated concentration (using 2.0×10^5 Da for MEH-PPV and 459.43 Da for Alq_3) was ~168 ppb for MEH-PPV and ~73 ppm for Alq_3. (c) Anthracene containing aerosol was generated by thermal evaporation. Anthracene is a white solid powder with a melting point of 210-215 °C. In this experiment, anthracene was thermal evaporated at 250 ºC. The evaporation rate was estimated to be 0.2 $mg \cdot s^{-1}$ by measuring the weight reduction. The carrier gas was 2000 sccm N_2. The calculated concentration (using 178.23 Da) was ~750 ppm. (d) 4-flourobenzenethiol and benzenethiol containing aerosol was generated using bubbler based evaporation. Specifically, the analyte was introduced using a conventional bubbler approach with a flow rate of 10 sccm N_2 in the bubbler line. The vapor pressure of 4-flourobenzenethiol is 2.85 mmHg and benzenethiol is 1.4 mmHg at room temperature which is equivalent of 3800 ppm of 4-FBT and 1800 ppm of BT molecules inside the bubbler and 19 ppm of 4-FBT and 9 ppm of BT after dilution with 2000 sccm N_2.

Fabrication of AgFON Substrate: Silicon wafers were first put in HF solution for 30 s to remove the native oxide. The wafers were rinsed in acetone, methanol, IPA, DI water, and further cleaned in piranha etch at 120 °C for 30 min, and then in 5:1:1 ratio of H_2O:NH_4OH:H_2O_2 for 30 min to make the surface hydrophilic. Surfactant-free, silica nanosphere suspensions (Bangs Laboratories, Inc.) was further diluted in ethanol (1:1

volume ratio), which served as a spreading agent. The suspension was dropped onto a water surface which yields a surface layer of silica beads. The Langmuir-Blodgett method was used to compact the beads and to transfer the beads to the target wafer. After drying the surface for 30 minutes, the AgFON standard substrate was completed through e-beam evaporation of 20 nm/180 nm Cr/Ag films to form the plasmonic cap layer.

SERS Characterization: SERS spectra and corresponding Raman microscopy intensity maps were acquired using a confocal Raman microscope system (Witec Alpha 300R) equipped with an objective lens (Nikon 100×, 0.90 NA in air). A fibre-optic interfaced 514 nm argon ion laser was used as a laser source, which was set to a constant power of ~2 mW for all SERS measurements in this report. The lateral imaging resolution of the confocal system considering the wavelength, and numerical aperture of the system is ~300 nm. The scattered light was analyzed using a 600 mm^{-1} spectrometer grating with a spectral resolution of about 3 cm^{-1}. The collection area was defined by a 5μm×5μm region with a 10×10 sampling density. The collection time for each sampling spot was 1 second. The reflectance absorption spectrum was analyzed using a VIS-NIR spectrophotometer (Ocean Optics, USB4000 VIS-NIR spectrometer, QR400-7-UV–vis reflection probe). The reflectance absorption spectrum of AgFON was collected and used for the chosen wavelength (514.5 nm).

Chapter V

Approaching Gas Phase Electrodeposition: Process and Optimization to Enable the Self-Aligned Growth of 3D Nano-Bridge-Based Interconnects

Jun Fang, Leslie Schlag, Se-Chul Park, Thomas Stauden, Jörg Pezoldt, Peter Schaaf, and Heiko O. Jacob

***Adv. Mater. 28**, 1770 (2016).*

5.1 Introduction

The formation of electrical connections between different points in space is a fundamental requirement in any device or system that requires the flow of current. As a consequence and depending on the scale, various free-standing point-to-point electrical wiring methods are used. [49-51] Freeform wires known at the macroscopic scales take on the shape of bondwires at the sub-mm scale, connecting chip-sized objects using wire diameters and contact pads, which can be as small as 10 μm and 20 μm, respectively. [52] An extension of free-standing point-to-point wiring to a truly microscopic or even nanoscopic scale, however, remains challenged. For example, a nanowire bonding process similar to what will be discussed does not yet exist. Instead, the microelectronics industry uses thin film technologies in combination with lithography to realize the required conductive traces, interconnects, or vias between device layers. [53, 54] This conventional approach has some disadvantages. First, these are monolithic "on chip" connections which cannot form freeform wire connection between disparate "off chip" parts of a system. Second, and in comparison to wire bonding, an extensive amount of lithographic steps, alignment, and registration is required to form relatively simple electrical connections. Moreover, the majority of the material (including Gold, Silver, or Copper) is wasted during evaporation of the metal and during lift-off or etching. As a consequence and with the aim to reduce material waste, research has been directed towards localized-selected-area-material-deposition concepts often under an umbrella termed as "printable electronics". [55-57] Serial-direct-write deposition techniques belong to this class. Direct write techniques commonly use a (i) liquid [58] or (ii) carrier gas [59] to transport the "electronic ink" to desired locations. Recently, researchers have fabricated free-standing graphene oxide and metallic bondwires to a truly microscopic or even nanoscopic scale. [60, 61] However, the process use an inkjet printing method, which requires individual registration of each bondwire. Consequently, the throughput of serial-direct-write remains challenged cannot satisfy the manufacturing requirement.

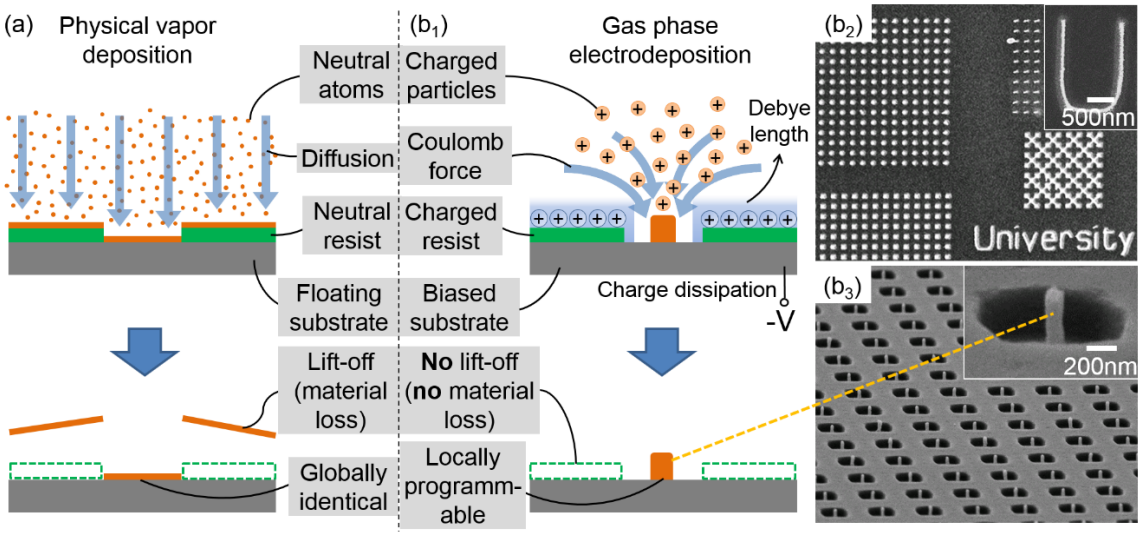

Figure 5-1. *Comparison between (a) conventional physical vapor deposition and (b) localized gas phase electrodeposition. (b_1) Under steady state operation the charged particles deposit locally in the charge dissipating opening. The insulating resist (green layer) has acquired a static surface charge distribution which yields fringing fields whereby the particles are funneled into the charge dissipating openings. No continued buildup of material on the insulating resist was reported as a result: (b_2) SEM image where the process was used to prepare a planar (2D) patterned metallic layer containing Au nanoparticles; (b_3) SEM image where the process was used to prepare 2.5D rod like deposit containing Pt nanoparticles.*

This publication will present a self-aligned nanowire bonding process [16] to form free-standing point-to-point electrical connections. Wire diameters down to 200 nm and contact pads down to 1 µm will be shown. Moreover, the process is a parallel process to achieve a higher throughput when compared with any of the emerging serial-direct-write or established serial wirebonding methods. The presented process is based on a method that is best referred to as "gas phase electrodeposition". The process has been described in parts before. [8] It is a localized material growth/deposition process which uses charged insulators to attract [17] or deflect [18] an incoming flux of charged material. This is illustrated in **Figure 5-1** which compares the recently discovered gas phase electrodeposition process with conventional physical vapor deposition. The starting point in both methods is a patterned photoresist or e-beam resist. However, on the right side the

material to be deposited (orange particles) is directed to the point of use and no material is lost in subsequent lift-off processes. Some previously reported structures are shown. [8]

Taking a closer look at the basic process, it becomes clear that gas phase electrodeposition shares some of the characteristics of electrodeposition in the liquid phase. However, it is a gas phase process with a much larger mean free path of the particles. The Debye length representing the screening length of Coulomb forces is also larger. [5] Despite this difference, it can grow nanostructures in selected domains in a programmable fashion by adjusting the dissipation current of the ionic species that arrive at the surface. For example, it was used to grow straight metallic nanowire arrays whose height and density were adjusted to vary across the substrate which in turn were used as contacts in photovoltaic devices. [9] Others have used this technique to fabricate metallic nanostructures for surface enhanced Raman spectroscopy (SERS). [5, 24] In any event, charged material continues to deposit into locations where charge dissipation can occur, leading to a growth of extended structures much like what is observed in the liquid phase based electrodeposition/plating.

This report evaluates the localized growth feature of gas phase electrodeposition as a method to form self-aligned free-standing nanowire interconnects. The optimization of the system is achieved by introducing an improved reactor to adjust the particle size and shape of the emerging structures, as well as electrical conductivity. The relationship between carrier gas flow, primary particle size, and packing density of the growing nanostructured deposits will be discussed and optimized since it led to an increase in the electrical conductivity of the nanostructured deposits when compared to prior results. Moreover, the growing structures can be manipulated by a local electric field to form various 3D geometries. Specifically, the process can be operated in a regime where the Debye length is further increased. As a consequence, it is possible to achieve an enhanced electrodynamic coupling between emanating and growing structures which we tailor to form electrical bridges, leading to the nanoscopic wirebonding idea extending the application ranges. Overall, we find that the gas phase electrodeposition provides an alternative to evaporation with several distinguishing attributes: it supports operation at atmospheric pressure (operation under vacuum is not required), the process is material efficient (material is

directed towards the point of use), and the process is locally programmable (instead of globally identical). As demonstrators, we choose the formation of freeform programmable point-to-point nano-bridge-based interconnects and the deposition of interdigitated electrode arrays.

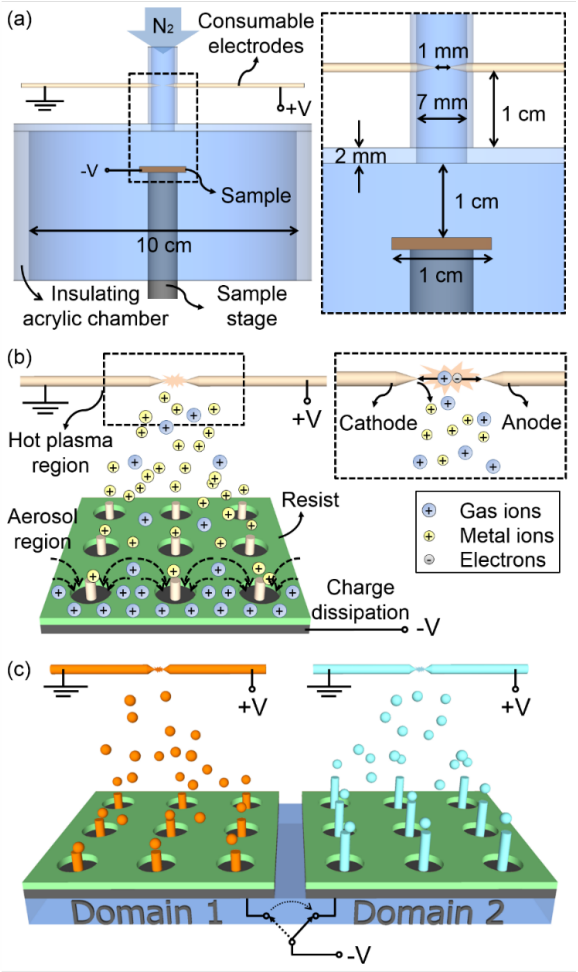

Figure 5-2. *Programmable gas phase nanomaterial electrodeposition system. (a) Current setup with dimensions detailing the carrier gas jet, the location of the consumable electrodes, the insulating chamber, and the sample stage. (b) Detailed gas phase electrodeposition process: the sample is patterned by an insulating resist (green) with openings to the underlying conducting domains (gray). The openings provide points where material will deposit/grow. The resist prevents charge dissipation and the material seeks to deposit in the openings. (c) Programmable electrodeposition concept: domain 1 is turned ON first for a certain deposition time leading to a desired structure (orange);*

domain 2 is turned ON in a second deposition cycle to receive and grow a different material for an extended period of time leading to a different structure (blue).

Figure 5-2(a) describes the programmable gas phase nanomaterial electrodeposition system used in this study. The system is in parts based on the original implementation [8] with the important exception (details discussed later) that it uses a carrier gas flow to transport the charged source material to the substrate and to reduce the particle size beyond previous levels. All the physical dimensions are different as well. The system is enclosed using a N_2 filled acrylic chamber which is kept at atmosphere pressure. The process uses a confined DC arc discharge between two closely spaced electrodes to produce nanoparticles through cathode erosion. The discharge leads to a plasma which surrounds the tip of the consumable cathode. For example, using the depicted 1 mm electrode gap an arc voltage of 1 kV is already sufficient to cause cathode erosion. The sample, typically a 1×1 cm^2 sized silicon or glass substrate with conducting domains is located downstream and collects charged particles.

Figure 5-2(b) provides details to explain the current understanding of the process. The sample is typically partially screened using a patterned thin layer of photoresist or e-beam resist (green) with openings to the underlying conducting domains (gray). The openings provide points where material will deposit/grow. The resist (green) prevents charge dissipation and the material seeks to deposit only in the openings. The process can be divided into (i) particle generation, (ii) charging, (iii) global transport, and (iv) localized selected area deposition.

(i) Particle generation: The process of particle formation through cathode erosion using atmospheric pressure arc discharge is well established. [62] Electrons generated in the plasma region are accelerated by the applied electric field to the anode, producing positive gas ions (blue) through impact ionization. The gas ions move and impact the cathode which leads to cathode erosion. We typically increase the voltage until an arc current of 2 mA is established; in nitrogen this will lead to ~1 kV voltage drop across a 1 mm gap, which is sufficient to achieve cathode erosion in the confined space. For example, after 100 hours and Au electrodes we recorded a cathode weight reduction of 3 mg. The resulting average

particle diameter is 3 nm (discussed later), which means that approximately 1.4×10^{14} particles are produced per hour to match the weight.

(ii) Charging: The eroded material (yellow) leaves the cathode surrounded by a positive space charge region and picks up positive charge resulting in the depicted particle; negative and neutral particles will be present as well (not shown).

(iii) Global Transport: in our particular situation, the arc region is modified through the application of a carrier gas jet, which is different from the previously reported design where no carrier gas was used. Previously we used diffusion based transport in combination with Columbic attraction of charged nanoparticles in close proximity to the substrate. The introduced carrier gas appears to play an important role in determining the nanoparticle size and affects the uniformity of the growing structures. Experimentally we find that the use of a carrier gas leads to the production of smaller particles, which will be discussed later. At the same time, it impacts the transport which is now dominated by the flow of the carrier gas transporting the particles towards the substrate.

(iv) Localized selected area deposition: This process is possible since all charged species are influenced by nearby electrodes. Depicted is the case for a negatively biased substrate (at a distance of ~2 cm, V_{sub} = -1000V is commonly used). The deposition process should be considered as an electrodynamic process since the localized field distribution will evolve over time. In the initial stage, an insulating surface will pick up a limited amount of charged material. This in turn will increase the electrical surface potential to reach equilibrium. The resulting electric field will deflect charged particles into the openings. Under steady state, a flux of positive charged material is established which flows to the conducting and bare electrode sites where charge dissipation is possible. Structures will grow only at sites where charge dissipation is possible. The resulting electrical domain current I_d is typically recorded with an electrometer (Keithley, model 6517A).

Moreover, it is possible to use the domain electrodes to collect material at different points in time or for a different duration. This is illustrated in Figure 5-2(c). Domain 1 is turned ON first for a certain deposition time leading to a desired structure length (orange, shown), or film thickness (not shown). Domain 2 is turned ON in a second deposition cycle

to receive and grow a different material for an extended period of time leading to a different structure (blue). No shutters are involved. This again is a possibility that does not exist in conventional vapor phase deposition processes where the entire substrate would be coated with a single layer.

5.2 Result

The optimization of the system in terms of reducing the average particle size and improving the nano structure is studied. Different from prior implementations, we used a carrier gas (N_2) in the current reactor. Experimentally we find that the use of a carrier gas leads to the production of smaller particles and growing structures that have an increased density and improved electrical conductivity.

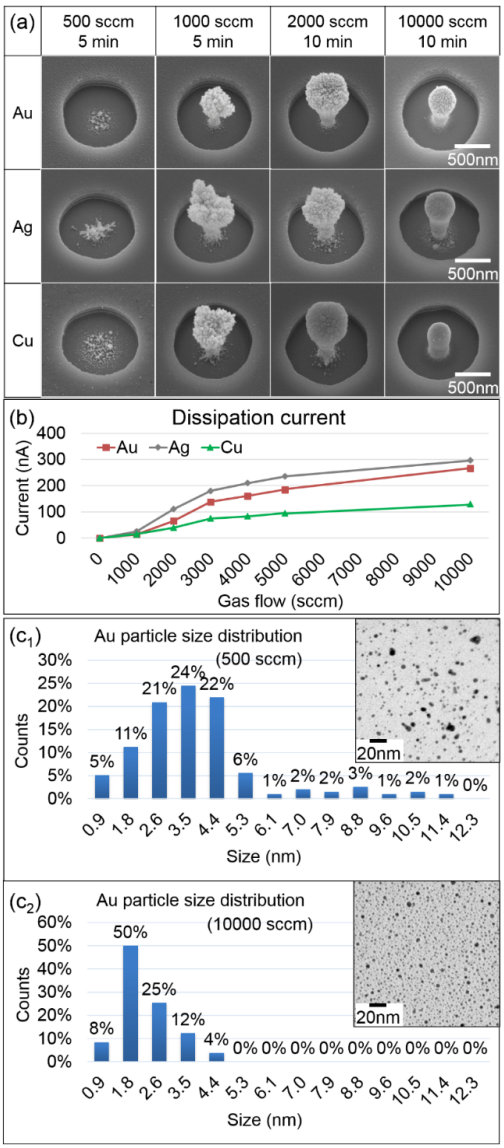

Figure 5-3. *Shape of the emerging structure, ionic substrate current, and primary particle size distribution as a function of carrier gas flow. (a) SEM images depicting Au, Ag and Cu deposits; the uniformity of the emerging structures improves with an increase in the carrier gas flow. (b) Graph of the dissipation current as a function of gas flow: a higher flow rate results in a larger dissipation current. (c) Histograms and TEM micrographs depicting the Au particle size distribution at (c_1) 500 sccm with 3.9 nm average diameter and 2.4 nm STD and (c_2) 10000 sccm with 2.2 nm average diameter and 0.8 nm STD.*

Figure 5-3 identifies the carrier gas flow as one of the key parameters in the optimization of gas phase electrodeposition since it affects the smoothness of the growing

structures. Specifically we discovered a clear dependence between carrier gas flow and (a) shape of the growing structures, (b) dissipation current at V_{sub} = -1000 V, and (c) particle size distribution. As mentioned before, the particles originate in the discharge region that is confined using a 7 mm inner diameter tube. The N_2 carrier gas was purchased from Matheson (UHP/ZERO GRADE, 99.999%). The gas flow rate was controlled by a digital gas flow meter. The temperature and the humidity in the experiment were set approximately to be 22°C and 50%, respectively. All metals we have tested show two operating regimes leading to either dendritic high surface-to-volume ratio structures or dense metallic deposits:

(i) "Low-carrier-gas-flow regime" represents the condition where a clear increase in the primary particle size (sometimes exceeding 10 nm) is observed and where the size distribution is larger. This in turn leads to a dendritic growth (***a***, left side). This statement is correct for all metals we have tested (shown: Au, Ag, Cu, not shown: Rh, In, Pt, Co, Mo, Re, Ru, Zn). These structures have a high surface-to-volume ratio and should be useful for any catalytic process, like batteries or cells for water splitting applications. [63] An exemplary histogram of the size distribution selecting the Au nanoparticles is shown (***c₁***). An average diameter (3.9 nm) and standard deviation (2.4 nm) was recorded in this case (experimental conditions were 500 sccm N_2, 2 mA arc current, 1 kV arc voltage, 8 nA dissipation current, and 10 min collection time, TEM analysis counting 100 particles collected on a TEM grit).

(ii) "High-carrier-gas-flow regime" represents the condition where a clear reduction in the primary particle size (typically smaller than 5 nm) is observed and where the standard deviation is reduced. This in turn leads to deposits and growing structures that are dense (***a,*** right side). Again all metals we have tested showed this behavior. These structures provide an increased mechanical stability and electrical conductivity (discussed later). An exemplary histogram of the size distribution selecting the Au nanoparticles is shown (***c₂***). Both the average diameter and standard deviation reduced from 3.9 nm to 2.2 nm and 2.4 nm to 0.8 nm, respectively (experimental conditions were 10000 sccm N_2, 2 mA arc current, 1 kV arc voltage, 260 nA dissipation current, and 10 min collection time, TEM analysis counting 100 particles collected on a TEM grit).

The discovered “carrier gas” –> “particle size” –> “structural and electrical property relationship” can be explained: With an increased carrier gas rate, an increased cooling rate around the arc region will be present, which should lead to smaller particles. Moreover, the arc shows more fluctuation leading to a visible movement of the “anchor” points at the electrodes at higher flow rates. As a consequence, the point of erosion will fluctuate and this should lead to shorter localized heating/erosion before the anchor point jumps to a new erosion point. In addition, the primary particles reach the sample surface faster, which should lead to a reduction in “arc & in-flight aggregation”. This explains the observed results: arrival of isolated round particles (***c*****2**, TEM insert) at high flow rates and a higher packing density.

The previously mentioned reduction of arc & in-flight aggregation is believed to be the primary factor to explain the increased packing density of growing structures in the high-carrier-gas-flow regime. This argument is also supported by the TEM images (***c***, inserts). At low-carrier-gas-flows and short exposure times (<1 min) we find isolated relatively large aggregates on the TEM grit. The size of these aggregates appears to be independent of the collection time. In other words, they must form in the arc region or in-flight before they arrive at the surface. For example, we tested 10s, 20s, and 40s and found >10 nm sized aggregates in each case which contained small (<3 nm) primary particles in the low-carrier-gas-flow regime. Growing structures, which are building up through continued collection of these large aggregated particles, are fluffy because of geometric hindrance. Furthermore, the recorded dissipation current is low despite the fact that the structures grow relatively quickly, which means that the charge/particle size ratio is much smaller in the low-carrier-gas-flow regime when compared to the high-carrier-gas-flow regime.

We believe that the suppression of arc & in-flight aggregation is the dominating factor in increasing the packing density in the high-carrier-gas-flow regime. However, another explanation exists which cannot be excluded. The second explanation considers the electrical mobility of charged particles. The current arrangement with a nozzle pointing down to the parallel plate is known to acts as a filter [64] that can attract particles based on the size or more specifically differential mobility. The arrangement favors charged particles with small diameter, which have a high electrical mobility, thus, are preferentially

attracted toward the surface. However, we do not believe that the effect of differential mobility plays an essential role in our case, otherwise we should see particle size gradient away from the center of the substrate collecting larger particles towards the edge. This is not observed. Moreover, we should see a reduction of the ionic current at higher flow rates since fewer particles will reach the surface. The opposite is the case. As a consequence, and for the reasons mentioned before, the suppression of arc & in-flight aggregation in the high-carrier-gas-flow regime is believed to be the primary reason why the packing density, structural stability, and electrical conductivity improve. In other words, the arrival of isolated and smaller particles is the primary reason.

To sum up, the optimization of the gas phase electrodeposition system is realized by introducing a carrier gas (N_2) in the current reactor, along with a redesigned reaction chamber. Both experimental results and theoretical analysis show that the generated particle size is reduced and the shape of the emerging structure is improved. This optimization provides a possibility to form point-to-point nano-bridge-based interconnects and interdigitated electrode arrays that will be discussed later.

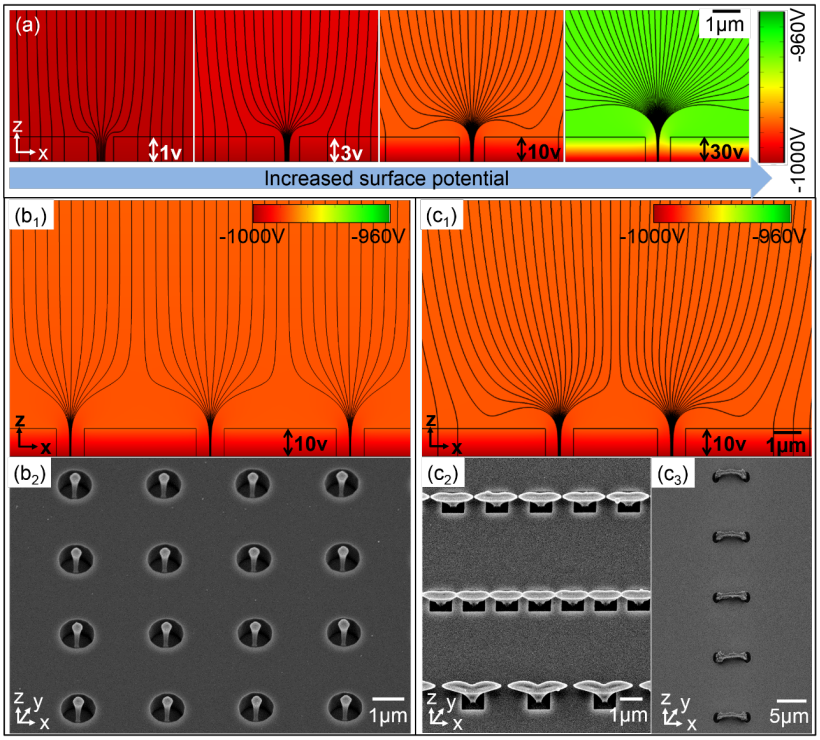

Figure 5-4. Nearest neighbor interaction - *Computed electric field distribution at different resist surface potentials (a) and localized gas phase electrodeposited copper structures comparing equally spaced (b, 5μm pitch) and unequally spaced (c) openings inside a 1 μm thick photoresist. An increase in the surface potential leads to an increased focus of the electric field lines. Unequal distances between nearest neighbors lead to the formation of copper bridges in the experiments. The upper and lower row (c_2) show and intermediate state where the bridge is not completely closed; 30 nm gaps (upper row) and 200 nm gaps (lower row) are visible; the gap distances are uniform from one location to the next. Wires bridging an 8 μm gap (c_3).*

Another interesting discovery deals with the screening length and nearest neighbor interaction. In the wet chemical electrodeposition, which shares some similarities, the Debye length is often used as measure to determine the screening length. It is commonly smaller than 10 nm and nearest neighbor interaction is limited. This is different in the discovered gas phase electrodeposition process. Nearest neighbor interaction can take place at much larger distances (10 μm in some cases). This supports a different set of applications. **Figure 5-4** provides some understanding on the effect of nearest neighbor interaction comparing computed electric field distributions with deposition results using a 1 μm thick photoresist (MICROPOSIT™ S1800™) with 1 μm sized openings to a Si substrate. The calculated field is shown for five different constant values (1V, 3V, 10V, 30V) of the surface potential; the actual level of the surface potential and distribution along the surface is unfortunately not known. From a computation point of view, an increase in the surface potential (4a, compare far right with far left image) leads to: (i) an increased focus of the electric field lines and (ii) fewer field lines which impinge on the insulating resist surface. The depicted impinging field lines are present at the outset of the experiment (4a, left). However, this will lead to a pick-up of positive charge, which in turn increases the surface potential and leads to a field distribution with fewer impinging field lines (4a, transitioning from left to right). In other words, in the experiments the insulating resist picks up positive ions and particles to a point where the surface potential has increased to a sufficiently large value to divert the flux of positive particles to the charge dissipating openings. A 1 μm thick layer of photoresist (MICROPOSIT™ S1800™) has a breakdown

strength of ~400 V/μm [65] and can thus float up to a sufficiently high value to divert the flux of charged particles.

This general behavior is visible in all experiments where the insulting resist is intact and not leaking. The shape of the growing structures (b and c) agrees well with computed field distribution (experimental conditions were: 2 mA arc current, 1 mm gaped copper electrodes, 10000 sccm of N_2, 130 nA ionic substrate current, and 10 min long deposition). Openings which are evenly spaced in the x and y direction (b) lead to a field distribution and growth pattern which points primarily in the z direction. Coupling to the nearest neighbors becomes visible as the growing structure leaves the photoresist guides, which can be used to grow asymmetric structures.

From a material deposition point of view, the observed growth behavior can be explained. It agrees with a material transport which arrives globally from the top in all cases. However, in Figure 5-4(c) the flux is divided into 2 dimensional sheets, which are in line with the rows of openings, before the sheets are broken down into individual filaments. This type of transport leads to the observed forking ($\mathbf{c_2}$) and ultimately to the formation of interconnects between nearest neighbors ($\mathbf{c_3}$).

The growth rate depends on various parameters. One of them is the density of the openings, which was approximately the same in (b_2 and c_2). The structures are about 2 µm long from the beginning to the end, which represents a growth rate of 200 nm/min. The number of openings per area was smaller in (c_3) leading to a slightly larger rate of approximately 400 nm/min. A different condition where the growth rate is >10 times higher will be discussed in the next paragraph.

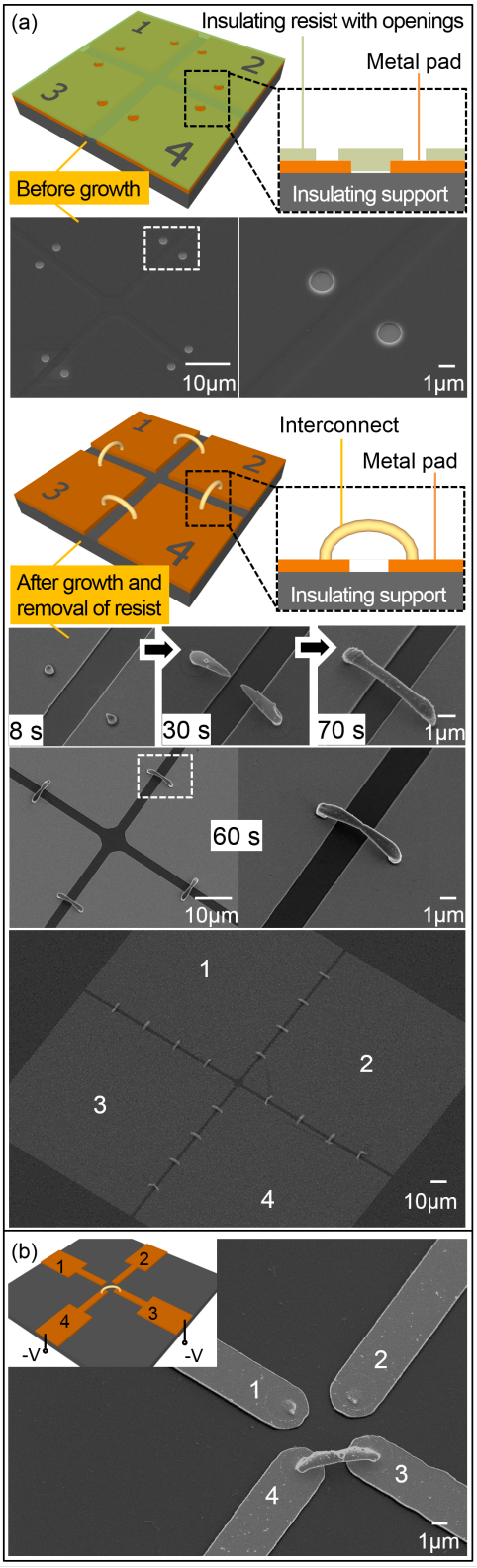

Figure 5-5. *Programmable growth of self-aligned free-standing nano-bridge-based interconnects: schematics and corresponding results before and after growth. (a) Nano-bridge-based interconnects applied to electrically connect 4 different 100 µm×100 µm squared metal pads. A 200 nm thick insulating PMMA resist (green layer) defines several 1 µm in diameter contact points with a 5 µm gap. SEM images after Au growth and removal of the resist showing the structures after 8 s, 30 s, 70 s, and 60 s long deposition. Overview SEM images showing a total of 16 (4×4) Au interconnects. (b) Nano-bridge-based interconnect grown in a programmable fashion. Metal pad 1 and 2 are left floating which prevents charge dissipation and continued growth (growth is turned OFF). Insert: Schematic of experiment and bias voltages, terminal 3 and 4 are biased negatively, growth is turned ON and electrodes 3 and 4 are connected with a 5 µm long Au nanowire.*

Figure 5-5 shows the schematics and corresponding results where the general strategy of gas-phase

nanoparticle electrodeposition is applied to grow self-aligned free-standing nano-bridge-based interconnects. A Si substrate with a 100 nm thick Si_3N_4 layer is used in this experiment. The insulating Si_3N_4 layer supports four contact pads. We use conventional e-beam evaporation Cr/Au (20nm/50nm) and photolithography to prepare these relatively large pads. The structure shows pairs of 1 μm in diameter contact points with one contact on each pad. The contact points are openings in an insulating 200 nm thick PMMA layer which we defined using e-beam lithographically. The goal was to grow freeform self-aligned nanowire bridges in between these locations. Results represent 2 mA arc current, 1 mm gaped Au electrodes, 10000 sccm of N_2, and 260 nA ionic substrate current. Interestingly, a 1 min long deposition time was sufficient to grow the bridge across the 5 μm long gap. In other words, the growth rate was 2.5 μm/min. This is a factor of ~12.5 higher when compared with the experimental results presented in Figure 5-4(b_2) and (c_2). The primary reason for the higher rate is the lower number of openings per area in the insulating resist where charge dissipation takes place. Generally speaking, the smaller the area and number of electrical contact points, the larger the growth rate. This is because the particle generation rate is constant. The observed behavior can be explained if all or most of the generated particles are collected. A smaller number of collection points lead to a higher localized material flux rate, resulting in a higher localized growth rate of the wires.

The grown structures and bridges were found to be fairly robust. We were able to remove the PMMA layer in acetone, washing the chips in IPA, and drying them under a stream of dry nitrogen without losing them. In Figure 5-5(a), all bridges were grown at the same time. The goal was to test the uniformity and the bridges looked alike in the SEM across the 200 μm×200 μm area. In Figure 5-5(b), the idea of programmable growth is tested. The goal was to evaluate if it is possible to grow a free-standing nano-bridge-based interconnect at a predetermined location. To achieve this goal, we applied a negative bias to terminal 3 and 4; at the same time we left terminal 1 and 2 floating. The deposition condition is identical to the previous experiment (2 mA arc current, 1 mm gaped Au electrodes, 10000 sccm of N_2, and 260 nA ionic substrate current, 1 min). Floating terminals block charge dissipation and growth at this location. Careful analysis, however, shows small amounts of unexpected precipitation on the floating pads 1 and 2. So some

charge dissipation must have taken place. A possible dissipation path could involve leakage through the 100 nm thin nitride layer.

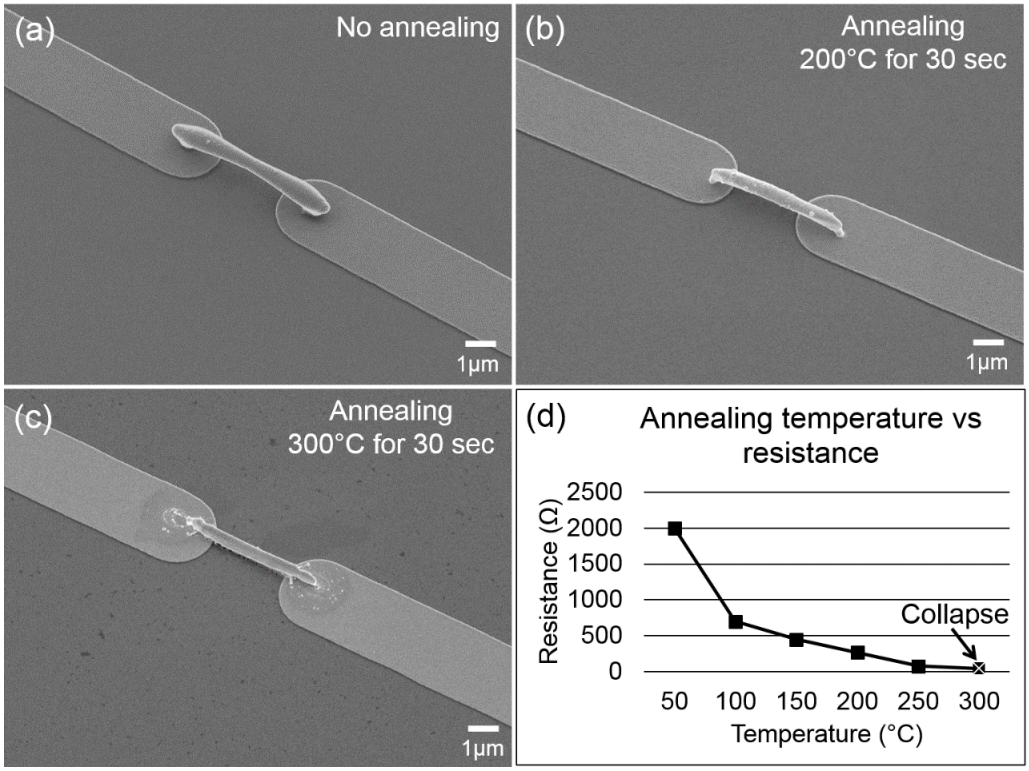

Figure 5-6*. SEM micrographs and total resistance of Au nano-bridge-based interconnects with and without annealing. SEM images (a) before and after a 30 s long annealing step at (b) 200 °C and (c) 300 °C in nitrogen; the bridges begin to break at 300 °C due to shrinkage. (d) A plot of resistances at different annealing temperatures.*

Figure 5-6 shows SEM micrographs of interconnects (a-c) next to a graph (d) of the measured resistance before and after annealing. The annealing is done in a rapid thermal annealer (RTP-600S, heated by tungsten-halogen lamps) under nitrogen. Results represent a nano-bridge-based interconnect spanning a 5 µm gap grown in 1 minute using the same conditions as described in Figure 5-5. Without annealing (a) the bridges had a fairly large resistance with values of a few kΩ, which is larger than what we hoped. However, a fairly small annealing temperature on the order of 200°C (b) is sufficient to reduce the resistance by a factor of 10 achieving less than 200 Ω. An annealing temperature of 250 °C has been determined as safe to maintain the integrity of the depicted interconnects leading to a

resistance of approximately 85 Ω or a factor of 23 when compared with the unannealed structures. These are the smallest values both in terms of required annealing temperature and achieved resistance we have achieved so far. The single most important parameter has been the reduction of the primary particle size. Prior structures which contained larger particle had a lower packing density and had poor electrical and mechanical properties. [9]

However, there is still room for improvement. The theoretical limit is 0.56 Ω (calculated using $R = \rho \cdot l/A$ with $l = 5\mu m$, cross-section $A = \pi \cdot (0.25\mu m)^2$, and $\rho_{Au} = 2.2 \times 10^{-8}$ Ω·m). We believe that a further reduction of the primary particle size is required to approach this limit. At present the particles have a diameter ranging from 1 to 5 nm. While the density has improved the growing structures are composed of nanoparticles and some level of porosity is likely remaining. In other words the structures have a higher level of porosity when compared to vapor deposition of single atoms. The assumption that some level of porosity is still remaining is consistent with the fact that a small amount of shrinkage is visible in the SEM images after heat treatment. For example, at 300 °C the shrinkage can lead to mechanical stress and subsequent failure of the attachment points and even collapse of the structures (c).

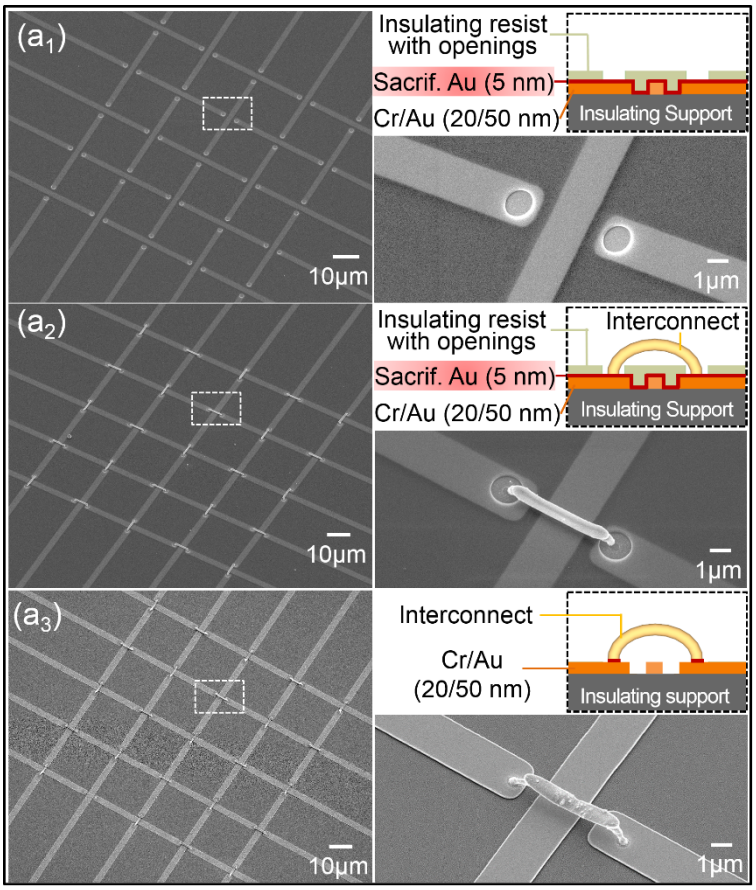

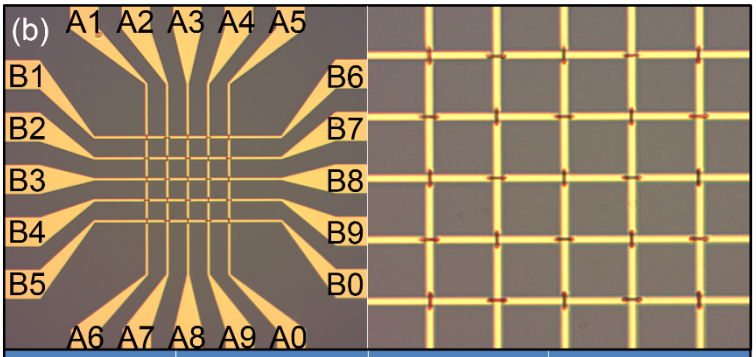

Columns A	Resistance	Rows B	Resistance
A1-A6	283 Ω	B1-B6	181 Ω
A2-A7	162 Ω	B2-B7	255 Ω
A3-A8	267 Ω	B3-B8	177 Ω
A4-A9	155 Ω	B4-B9	248 Ω
A5-A0	239 Ω	B5-B0	150 Ω
$A_i - B_j = \infty$			

Figure 5-7. *Gas phase electrodeposition applied to grow self-aligned interdigitated electrode arrays: SEM images, optical micrographs and resistance values. SEM images show the test structure with 25, crossovers (a_1) before growth, (a_2) after growth, and (a_3) after removal of the resist and Au sacrificial layer. Each bridge growth across the intersecting electrode without touching it. (b) The table lists the total resistance measured between the terminals depicted in the overview optical microscope image; on average a bridge contributes 85 Ω to the total resistance which is either 170 Ω or 250 Ω depending on the number of crossovers in the daisy chain. A_i - $B_j = \infty$ means that no leakage current was detected between the columns and the rows.*

Figure 5-7 shows micrographs of a 5×5 interdigitated electrode array test structure which requires the growth of 25 isolated crossovers between the rows and columns. The rows and columns are on the same layer. Two ideas are being tested. The first idea is to evaluate if crossovers can be fabricated with fewer processes and alignment steps than commonly necessary. Conventional realization of crossovers requires: (i) deposition; registration and patterning of an insulator; (ii) via plating and polishing; and (iii) deposition, registration, and patterning of a top conductive layer. In comparison, our approach replaces steps (ii-iii) with a single registration-free gas-phase-electrodeposition step. The second idea behind the design is to test if daisy chains of bridges lead to a total resistance which is a multiple of the resistance of an individual interconnecting bridge as previously recorded in Figure 5-6. Consequently, the same processing conditions were used in this experiment with one exception. Specifically, the test structure contains several strips of metallic conductors (electrically isolated sections of rows and columns). No electrical bias can be applied to these regions and charge dissipation and growth will not occur. As a result, the concept of gas phase electrodeposition is not possible in these areas. However, a solution from the wet chemical counterpart can be borrowed. Like in wet chemical electroplating a thin sacrificial charge dissipating metallic layer (red layer in the inserts) underneath the resist (green layer) is required to plate metal at the locations where the vias are present. We used a 5 nm thin layer of evaporated Au to support temporary charge dissipation and crossover nanowire growth (a_1). Like in previous experiments, the nanowires are grown within 1 minute with the same deposition condition (a_2). Subsequently the PMMA layer is removed in Acetone and the substrate is immersed in GE-6 gold etchant for 10 s to remove the thin gold sacrificial layer. The nanowires remain intact due to a short etch time. The samples are annealed at 250 °C for 30 seconds leading to the final structure (a_3). Figure 5-7(b) shows an overview optical microscopy image with overlaid pad labels and a table with measured values of the total resistance. The measured total resistance depends on the number of crossovers in each daisy chain. Depending on the location of the row or column there are either two or three crossovers in this array. Out of the 25 crossovers all were electrically intact. On average, each crossover accounts to about 85 Ω. Moreover, no electrical shorts between the columns and rows were detected indicating that the crossovers are not in contact with the electrodes underneath.

5.3 Conclusion

A novel nanowire bonding processes to grow free-standing point-to-point electrical connections has been demonstrated. The process is based on a gas phase electrodeposition concept, which is a localized material growth/deposition process where a patterned insulating resist is used to control charge dissipation. The process is more material efficient when compared to conventional vapor deposition since the material is directed to the point of use. No lift off is required.

The nanoparticles were produced using an arc discharge based plasma. Here the use of a carrier gas was discovered as an important parameter to reduce the primary particle size below a 3 nm threshold. Moreover, the carrier gas reduced in-flight-aggregation which in turn improved the density, mechanical, and electrical property of the growing nanostructures. Electrical measurements are now possible due to the improved mechanical and electrical characteristics.

The resistivity in the case of Au deposits is presently about 7.9×10^{-5} Ω·m without annealing and 3.3×10^{-6} Ω·m with annealing at 250°C (calculated using the measured resistance and dimensions l = 5μm and r = 250nm). While it is the first time electrical measurements have been reported the values are still by a factor of 150 higher than the bulk resistive 2.2×10^{-8} Ω·m of gold indicating that there is room for improvement. We believe that a reduction of the primary particle size into the sub 1 nm range is likely going to continue to improve the electrical and mechanical properties. However, the exact methodology how to achieve the required reduction in the primary particle size is not yet known. Possible solutions could be an increase in the gas flow beyond the levels reported in this publication, the use of a different or cooled carrier gas, changes in the localized flow velocity surrounding the arc region, a reduction of the arc power, and changes in the pressure. The study and optimization of this parameter space requires the design of an improved gas phase electrodepositing system. Alternatively, a further improvement of the conductivity and mechanical properties could be achieved through an in-situ annealing approach; for example, through the incorporation of a flash lamp annealing methodology, or a temperature controlled and heated substrate or deposition chamber.

The discovered nearest neighbor coupling effect supports the growth of bridges. The growth of bridges is possible due to an increased screening length when compared to the wet chemical counterpart where a high ion concentration screens charges within a few nm. Nearest neighbor coupling across a 10 μm gap has been possible. This finds applications. The demonstrated freeform programmable point-to-point nano-bridge-based interconnects, and the deposition of interdigitated electrode arrays are two examples. In the future it should be possible to extend this further, it should be possible to create 3D free-standing nanowire structures and freeform wire connection between disparate "off chip" parts of a system. The formation of vias between device layer through gas-phase deposition should also be possible.

While the applications are apparent we feel that the understanding of the deposition process remains fairly limited. The effect of pressure, carrier gas temperature, substrate temperature, gas ion concentration, insulting resist type and thickness, and humidity on the growth process for example is not known. The ultimate level of precision or conductivity that can be reached is also not known.

5.4 Experimental Section

***Chamber and Arc Discharge*:** The current setup (Figure 5-2) uses a carrier gas jet with gas flow rates between 20 and 20000 sccm nitrogen. The gas inlet has 7 mm inner diameter. The consumable electrodes are located in the carrier gas jet inlet 10 mm in distance to the insulating chamber. The inner diameter of this chamber is 100 mm. The walls are at least 2 mm thick. The sample stage is located 10 mm underneath the gas inlet, 20 mm in distance from the consumable electrodes. The applied electrical current between anode and cathode is 2 mA, in nitrogen this will lead to 1 kV voltage drop across a 1 mm gap. After 100 hours and Au electrodes the cathode weight reduction is 3 mg. Various types of metals were used, we tested Au, Ag, Cu, Rh, In, Pt, Co, Mo, Re, Ru, and Zn. The metals were ordered as wires with 1 mm diameter at Advent Research Materials. Except the Ru, which is just available at Goodfellow as bridle 2 mm x 2 mm thick bar. The corresponding dissipation currents at specific gas flow rates are shown for Au, Ag, and Cu in Figure 5-3. The resulting electrical dissipation current, I_d is recorded with a Keithley, model 6517A.

Particle Size Distribution: The particles were collected on Quantifoil® S7/2 copper 300 mesh substrates. This foils were analyzed by a TEM TECNAI model S20 with Gatan filter. Particles were man-counted and man-measured in an area of 500 nm x 500 nm at different sites of these foils. The resulting average particle diameter is 3 nm, which means that approximately 1.4×10^{14} particles are produced per hour to match the weight.

Substrate Preparation: To grow metallic nanowire directly on Si wafer, the Si wafer (P-type, 0-100 Ω·cm) was cleaned by acetone, IPA and DI water. The wafer was then patterned by photoresist (MICROPOSIT™ S1800™). The thickness of the photoresist depends on the spin speed during the coating process. To form nano-bridge-based interconnects on the substrate, a Si_3N_4 insulating layer (1000 Å) was first grown on Si wafer. Conventional e-beam evaporation and photolithography was used to prepare Cr/Au (20nm/50nm) layer. E-beam lithography was then used to pattern PMMA insulating layer with openings at desired location.

Chapter VI

Gas Phase Electrodeposition and Growth of Free-Standing Point-to-Point Electrical Connections and Microscopic Bondwires

Jun Fang, Leslie Schlag, Se-Chul Park, Thomas Stauden, and Heiko O. Jacobs

Manuscript Submitted, (2016).

6.1 Introduction

The formation of electrical connections between different points in space is a fundamental requirement in any device or system that requires the flow of current. As a consequence and depending on the scale, various free-standing point-to-point electrical wiring methods are used. [49-51] Freeform wires known at the macroscopic scales take on the shape of bondwires at the sub-mm scale. Conventional bondwires connect chip-sized objects. However, wire diameters and contact pads should be larger than 10 and 20 μm, respectively. [52] An extension of free-standing point-to-point wiring to a truly microscopic or even nanoscopic scale, however, has not been demonstrated. For example, a nanowire bonding process similar to what will be discussed does not yet exist. Earlier attempts have focused on the seeded and directed growth of nanowires primarily through chemical vapor deposition (vapor solid or vapor liquid solid) growing carbon nanotubes [66] and nanowires out of Si, [67] GaN [68] and ZnO, [69] to name a few. Orientation between contacting areas was based on the use of a lattice matched crystal facets. Growth across a trench etched inside a Si wafer [70] or a via and vertical interconnect between one device layer to another [71] was achieved. However, the direction of growth was primarily unchanged and unidirectional. [16] Reports on the growth of curved bridges between predetermined contact points on the other hand are limited. For example, Tian et al. used hierarchical nanowires that were constructed using a nanotectonic approach analogous to metal–organic framework materials. [72] Another exception is the work by McEuen et al. who used an electric field to direct the growth in the case of carbon nanotubes. [73] This process however was a high temperature CVD growth process which is different from what will be discussed. In addition, the structures were not metallic.

This article will present a self-aligned nanowire bonding process which forms free-standing point-to-point electrical connections. The presented process is based on a method that is best referred to as “gas phase electrodeposition”. The process has been described in parts before. [5, 6, 8, 17, 18] The relevant elements as they are known so far are briefly described to put the current research in context. First it is a localized material growth/deposition process which uses charged insulators to attract [17, 18] or deflect [5, 6] an incoming flux of charged material. The gas phase electrodeposition process shares

some of the characteristics of electrodeposition in the liquid phase. However, it is a gas phase process with a much larger mean free path of the particles. The Debye length representing the screening length of Coulomb forces is also larger. [8] Despite this difference, it can grow nanostructures in a programmable fashion by adjusting the dissipation current of the ionic species that arrive at the surface of externally biased electrodes. For example, in the simplest case it was used to grow straight metallic nanowire arrays whose height and density were adjusted to vary across the substrate, which in turn were used as contacts in photovoltaic devices. [9] Others have used this technique to fabricate metallic nanostructures for surface enhanced Raman spectroscopy (SERS). [5, 24] In any event, charged material continues to deposit on locations where charge dissipation can occur, leading to a growth of extended structures much like what is observed in wet chemical electrodeposit ion/plating.

6.2 Material and methods

This article establishes the operating conditions required to grow self-aligned free-standing nanowire interconnects/bridges. The gas phase electrodeposition process uses a patterned resist with openings to a conductor to guide the deposition of charged nanoparticles. Nanowire growth occurs at charge dissipating contact points and the formation of nano-interconnects/bridges through nearest neighbor interaction is possible. The nanowires are composed of metallic nanoparticles. It was required to reduce the primary nanoparticles size to the 1-5 nm range to achieve electrical conductive and mechanically stable interconnects.

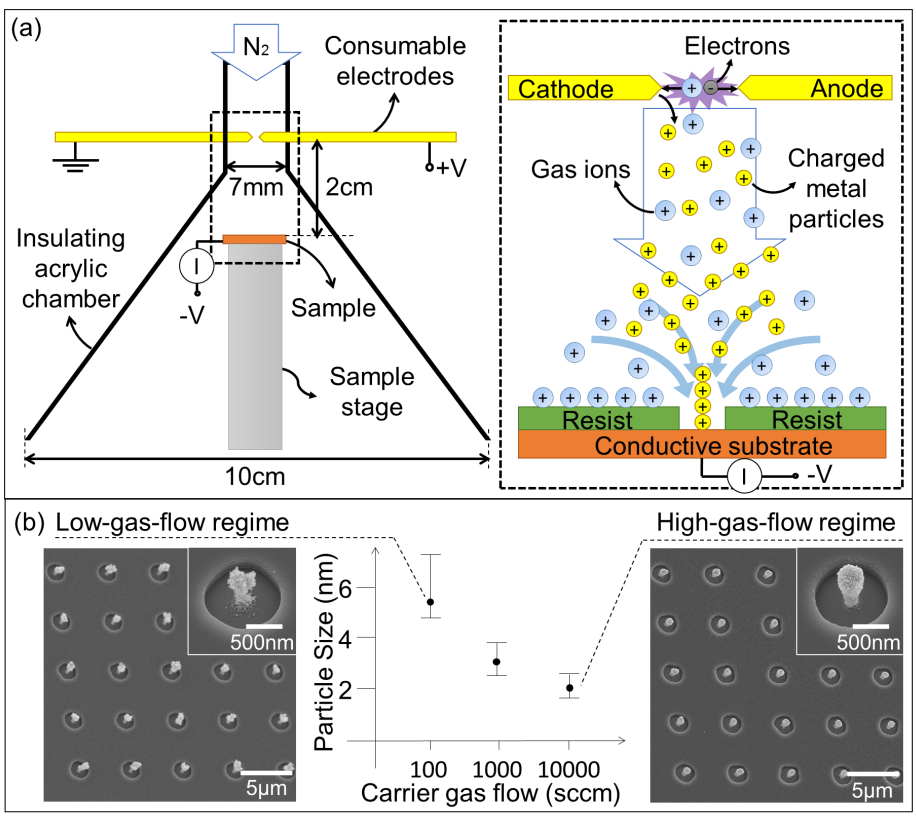

Figure 6-1. *Gas phase nanomaterial electrodeposition: basic concept and vertical growth result at low and high gas flow rates. (a) Dimension of the deposition chamber detailing the carrier gas jet, the arc discharge region, the two consumable electrodes (Au in this study), and the sample stage. The charged metallic nanoparticles (yellow) originate through cathode erosion in the plasma region (purple, inset). A carrier gas (N_2) provides*

cooling and transport. Positively charged particles and gas ions move to the negatively biased substrate (brown). The insulating resist (green, insert) prevents charge dissipation and the material seeks to deposit in the charge dissipating electrically biased openings. (b) Particle size histograms and SEM micrographs depict the deposition of Au particles at a low and high carrier gas flow regime. The Au particle size reduces with an increase in the carrier gas flow, resulting in an improved uniformity of the emerging structures.

Figure 6-1(a) describes the gas phase nanomaterial electrodeposition system used in this study. Different from the original implementation, [8] the recently developed system introduces a carrier gas flow to reduce the particle size beyond previous levels (discussed later) and to transport the charged source material to the substrate. All the physical dimensions are different as well. The system is enclosed using a N_2 filled funnel-shaped acrylic chamber which is kept at atmospheric pressure. The process uses a confined DC arc discharge between two closely spaced electrodes to produce nanoparticles through cathode erosion. The discharge leads to a plasma which surrounds the tip of the cathode. For example, using the depicted 1 mm electrode gap, an arc voltage of 1 kV is sufficient to cause cathode erosion. The sample, typically a 1×1 cm^2 sized silicon or glass substrate with conducting domains is located downstream to collect the charged particles. The insert provides details to explain the current understanding of the process. The sample is partially screened using a patterned thin layer of resist (green) with openings to the underlying conducting domains (brown). The openings provide points where material will deposit/grow. The resist (an insulator) prevents charge dissipation and the material seeks to deposit only in the openings to the conductive domains/contacts. The process of particle formation through cathode erosion using atmospheric pressure arc discharge is well established. [62] In brief, electrons generated in the plasma region are accelerated by the applied electric field to the anode, producing positive gas ions (blue) through impact ionization. The gas ions move and impact the cathode which leads to cathode erosion. The eroded material (yellow) leaves the cathode that is surrounded by a positive space charge region and picks up positive charge resulting in the depicted particles. Negative and neutral particles will be present as well (not shown). The gas ions and particles are then transported to the negatively biased substrate by the carrier gas (N_2). In the initial stage the insulating resist will pick up gas ions and a limited amount of charged particles. This in turn will

increase the electrical surface potential to reach equilibrium. The resulting electric field will deflect charged particles into the openings. Under steady state, a flux of positively charged material is established which flows to the conducting and bare electrode sites where charge dissipation is possible. Structures will grow only at sites where charge dissipation is possible. The resulting dissipation current on the substrate I_d is recorded with an electrometer (Keithley, model 6517A).

Figure 6-1(b) shows a histogram of the average particle size and corresponding structures in terms of different carrier gas flows. With the introduction of the carrier gas the gold particle diameter and STD can be reduced by about a factor of 2. For example, at low carrier gas flow we record an average diameter of 5.2 nm and STD 2.6 nm. With the introduction of the carrier gas, the numbers reduce to 2.2 nm and STD 0.8 nm (experimental conditions: 2 mA arc current, 1 kV arc voltage, 260 nA dissipation current, and 10 min collection time, comparing 100 with 10000 sccm N_2), resulting in an improved uniformity of the emerging structures. The discovered "carrier gas" –> "particle size" –> "structural property" can be explained: With an increased carrier gas flow rate, an increased cooling rate around the arc region will be present which should lead to smaller particles. Moreover the arc shows more fluctuation leading to a visible movement of the "anchor" points at the electrodes at higher flow rates. As a consequence, the point of erosion will fluctuate and this should lead to shorter localized heating/erosion before the anchor point jumps to a new erosion point. In addition, the primary particles reach the sample surface faster at a high gas flow rate, which should lead to a reduction in "arc & in-flight aggregation".

Another interesting discovery deals with the screening length and nearest neighbor interaction. Different from the wet chemical electrodeposition, a clear nearest neighbor interaction can be observed in our process. This is not the case in wet chemical electrodeposition due to a Debye screening length which is commonly smaller than 10 nm. However, in the discovered gas phase electrodeposition process, the nearest neighbor interaction can take place at much larger distances (10 μm in some cases). This supports a different set of applications. **Figure 6-2** provides some understanding on the effect of nearest neighbor interaction comparing computed electric field distributions with deposition results using a 0.5 μm thick photoresist (Microposit 1805) with 1 μm sized

openings to a Si substrate. The calculated field is shown for three different constant values (1V, 10V, 100V) of the surface potential difference with a -1000V substrate bias. The actual level of the surface potential and distribution along the surface is unfortunately not known. From a computation point of view, an increase in the surface potential difference (Figure 6-2(a), top) leads to: (i) an increased focus of the electric field lines and (ii) fewer field lines which impinge on the insulating resist surface. In other words, in the experiments the insulating resist picks up positive ions and particles to a point where the surface potential has increased to a sufficiently large value to divert the flux of positive particles to the charge dissipating openings. Microposit S1805 photoresist has a breakdown strength of ~400 V/μm and can thus float up to a sufficiently high value to divert the flux of charged particles. [65] This general behavior is visible in all experiments where the insulating resist is intact and not leaking. The shape of the growing structures agrees well with the computed field distribution (experimental conditions were: 2 mA arc current, 1 mm gaped Au electrodes, 10000 sccm of N_2, 130 nA ionic substrate current, and 3 min long deposition). In Figure 6-2(b) left where the openings are evenly spaced in the x and y direction, the growth pattern points primarily in the z direction. An exception is the edge of the pattern where the nanowire structures tilt towards the center due to an asymmetric distribution of electric field. This behavior matches the computation result (Figure 6-2(a), bottom). In Figure 6-2(b) right, the openings in x direction are more closely patterned than y direction, thus, the flux is divided into 2 dimensional sheets in x direction, which are in line with the rows of openings before the sheets are broken down into individual filaments. This type of transport leads to the observed forking. The self-assembly of free-standing nano-interconnects and nano-bridges that will be discussed later is based on this observed growth behavior.

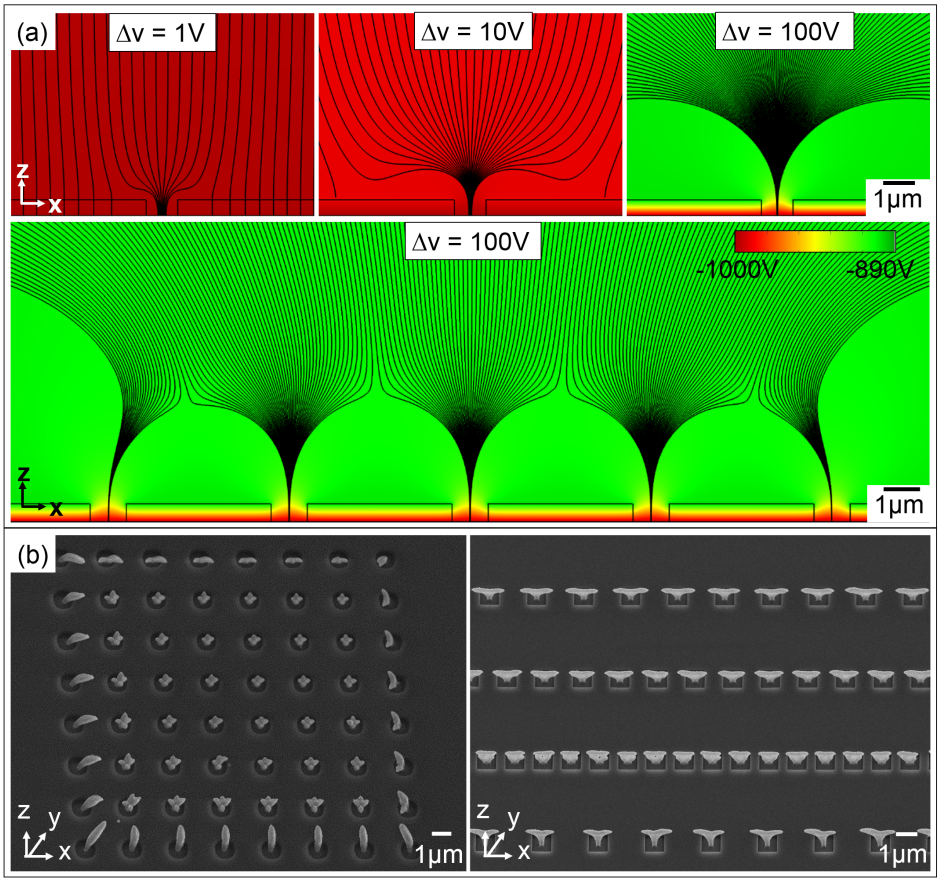

Figure 6-2. *Nearest neighbor interaction. (a) Computed electric field distribution at different resist surface potentials. An increase in the surface potential leads to an increased focus of the electric field lines. The distribution of electric field varies depending on the layout of the openings. (b) Localized gas phase electrodeposited Au structures comparing equally spaced (left, 3μm pitch) and unequally spaced (right) openings inside a 0.5 μm thick photoresist. The nanowire structures at the edge of the pattern will lean to the center due to the asymmetric distribution of electric field. Unequal distances between nearest neighbors lead to the formation of forking structures.*

6.3 Results

Figure 6-3(a) shows the schematics and corresponding results where the general strategy of gas phase nanoparticle electrodeposition is applied to grow self-aligned free-standing nano-interconnects. A Si substrate with a 100 nm thick Si_3N_4 layer is used in this experiment. The insulating Si_3N_4 layer supports two contact pads. We used conventional e-beam evaporation Cr/Au (20nm/50nm) and photolithography to prepare these relatively large pads with a size of 50 µm by 50 µm with a gap of 2µm between each pad. The structure shows pairs of 1 µm in diameter contact points with one contact on each pad. The contact points are openings in an insulating 200 nm thick PMMA layer, which we defined using e-beam lithography. These openings can also be prepared using conventional photolithography or nano-imprint lithography. However, we prefer to use e-beam lithography since we can test new designs within one day; no chrome mask or imprint stamp is needed.

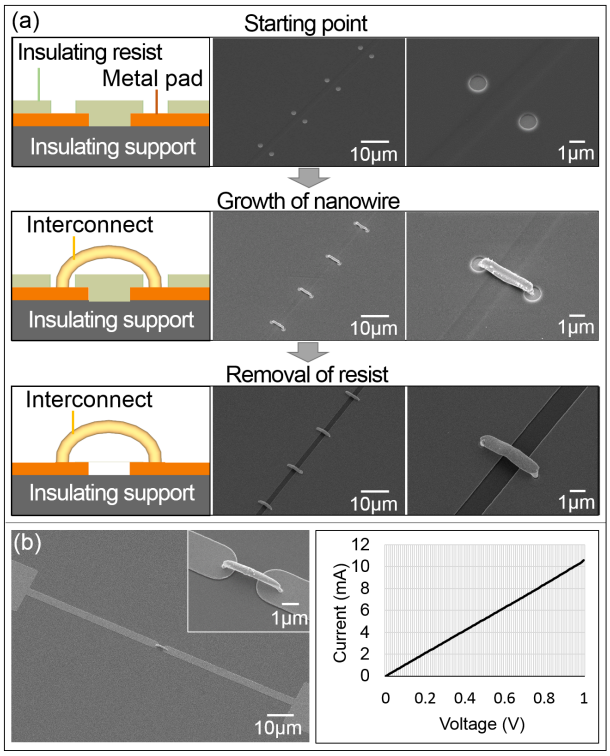

Figure 6-3. *Growth of self-aligned free-standing nano-interconnects and I-V characterization. (a) Schematics and corresponding results before and after growth: nano-*

interconnects applied to electrically connect two different metal pads. A 200 nm thick insulating PMMA resist (green) defines several 1 μm in diameter contact points with a 5 μm gap. Overview SEM images showing a total of 4 Au interconnects. (b) SEM micrographs and I-V characterization of Au nano-interconnects after annealing.

The Results represent 2 mA arc current, 1 mm gaped Au electrodes, 10000 sccm of N_2, and 260 nA ionic substrate current. A 1 min long deposition time was sufficient to grow the bridge across the 5 μm long gap due to the lower number of openings per area in the insulating resist where charge dissipation takes place. All interconnects were grown at the same time. The interconnects were found to be fairly robust. We were able to remove the PMMA layer in acetone, washing the chips in IPA, and drying them under a stream of dry N_2 without losing them. By using the carrier gas to reduce the particle size, the nanowires have been improved to a point that the structures remain stable during the post processing. At present, the longest point-to-point freestanding bridges we present are 5 μm long. In principle, we have been able to grow longer self-aligned point-to-point electrical connections using the process.

6.4 Discussion

In order to test the electrical properties, a single nanowire was grown across two metal domains. Figure 6-3(b) shows SEM micrographs of interconnect (left) next to a graph (right) of the measured I-V curve after annealing. The annealing is done in a rapid thermal annealer (RTP-600S, heated by tungsten-halogen lamps) under N_2. Results represent a nano-interconnect spanning a 5 μm gap using the same conditions as described before. The interconnect has a fairly large resistance with values of a few kΩ before annealing, which is larger than what we hoped. However, an annealing temperature on the order of 250°C is sufficient to reduce the resistance to the depicted level in the I/V curve, which represents 85 Ω. This represents the smallest values both in terms of required annealing temperature and achieved resistance. Prior structures which contained larger particle had a lower packing density and had poor electrical and mechanical properties. In fact, previously we were not able to grow mechanically stable bridges, which would survive the acetone washing process, and no electrical measurement could be taken. However, there is still

room for improvement. The theoretical limit is 0.56 Ω (calculated using $R = \rho \cdot l/A$ with $l = 5\mu m$, cross-section $A = \pi \cdot (0.25\mu m)^2$, and $\rho_{Au} = 2.2 \times 10^{-8}$ Ω·m). We believe that a further reduction of the primary particle size is required to approach this limit. At present the particles have a diameter ranging from 1 to 5 nm. While the density has improved, the growing structures are composed of nanoparticles and some level of porosity is likely remaining. In other words the structures have a higher level of porosity when compared to vapor deposition of single atoms. The resistance value is largely independent of the length of the wires, which means it is dominated by the contact to the substrate. For example, we did characterize point-to-point electrical Ni connections with different lengths. A 60% increase in the length lead to an 8% increase in the resistance; the contact to the substrate is clearly the week point both electrically and mechanically.

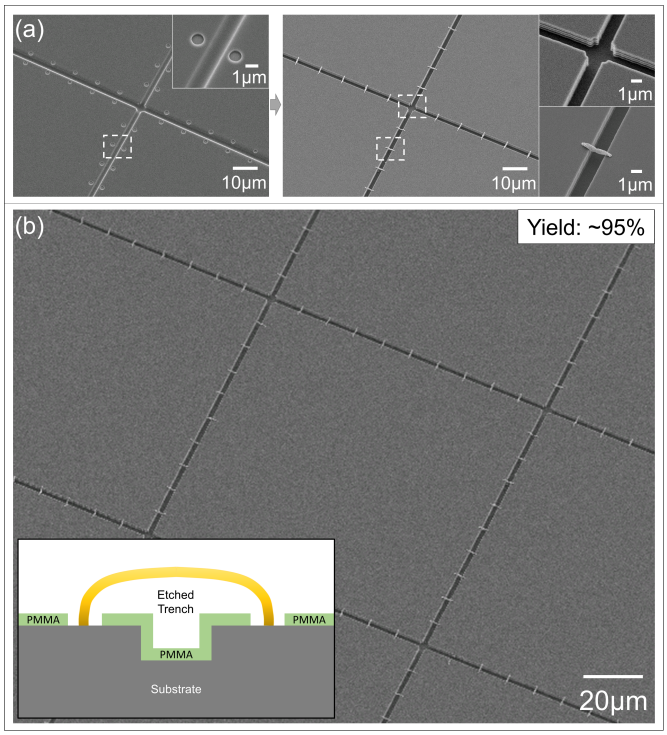

Figure 6-4. *Gas phase electrodeposition applied to grow an array of self-aligned nano-bridges across 1 µm deep and 2 µm wide trenches in Si. (a) SEM close-ups before and after growth. (b) Large area overview and cross section of the structures: 95% of the bridges are intact.*

Figure 6-4 shows results of gas-phase electrodeposition applied to grow self-aligned nano-bridge arrays across 1 μm deep and 1 μm wide trenches in Si. A Si wafer was patterned and etched by deep trench etcher (SLR -770) to form 1 μm deep and 2 μm wide trenches. Similar to the previous experiment, multiple pairs of 1 μm in diameter contact points with one contact on each side were patterned by an insulating 200 nm thick PMMA layer defined by e-beam lithography (see inserts in (a)). The free-standing nano-bridge structures are formed using the same experimental condition as described before (2 mA arc current, 1 mm gaped Au electrodes, 10000 sccm of N_2, and 260 nA ionic substrate current, 1 min long deposition 95% of the 5 μm long freestanding bridges survived the removal of the PMMA layer in acetone. This number can likely be improved with an increased deposition time as this would lead to a larger diameter and improved mechanical strength. However, at present the diameter is 250 nm and we loose 5% of the wires due to mechanical detachment during the washing process in Acetone. The detachment always occurs close to the interface (foot region) between the contact pad and the bridge.

We did test the growth of longer self-aligned freestanding point-to-point bridges. The yields presently drop to 60%, 10%, and 0% if the points are 10 μm, 15 μm, and 20 μm apart, respectively. We should mention that the self-aligned growth process works over distances that exceed 20 μm; however, they do not survive the post processing. Improvements in the mechanical strength and electrical properties of the attachment points are critically important going forward. Moreover, advanced "gentle" resist removal techniques such as critical point drying could offer a potential solution.

6.5 Conclusion

A novel nanowire bonding processes to grow free-standing point-to-point electrical connections has been demonstrated. The process is based on a gas phase electrodeposition concept, which is a localized material growth/deposition process where a patterned insulating resist is used to control charge dissipation. Like most patterning techniques a patterned resist is required to define the structures. However, the discovered gas-phase electrodeposition process differs from conventional vapor phase deposition techniques like evaporation where material is deposited uniformly on the substrate surface and reactor

walls without localization. Instead the process is more material efficient since the material is directed to the point of use. As a consequence, no lift-off is required. Moreover, freeform bridges can be formed using a nearest neighbor coupling effect. As a material source nanoparticles are used instead of atomic metal vapor. The nanoparticles are produced using an arc discharge based plasma. Here the use of a carrier gas was discovered as an important parameter to reduce the primary particle size below a 3 nm threshold. Moreover the carrier gas reduced in-flight-aggregation which in turn improved the density, mechanical, and electrical property of the growing nanostructures. Due to the improved mechanical and electrical characteristics, it was possible to report on the electrical properties of the growing structures. The resistivity in the case of Au deposits is presently about 7.9×10^{-5} Ω·m without annealing and 3.3×10^{-6} Ω·m with annealing at 250°C (calculated using the measured resistance and dimensions l = 5 μm and r = 250 nm). While it is the first time electrical measurements have been reported, the values are still a factor of 150 higher than the bulk resistive (2.2×10^{-8} Ω·m) of gold, indicating that there is room for improvement. We believe that a reduction of the primary particle size into the sub 1 nm range is likely going to improve the electrical and mechanical properties further.

We discovered a nearest neighbor coupling effect which supports the growth of bridges. The growth of bridges is possible due to an increased screening length when compared to the wet chemical counterpart where a high ion concentration screens charges within a few nm. Nearest neighbor coupling across a 10 μm gap has been observed. This finds applications. The demonstrated freeform point-to-point nano-interconnects and nano-bridges are two examples. In the future it should be possible to extend this further to create 3D free-standing nanowire structures and freeform wire connection between disparate “off chip” parts of a system. The formation of vias between device layers through gas phase deposition should also be possible. While the applications are apparent, we feel that the understanding of the deposition process remains fairly limited. The effect of pressure, carrier gas temperature, substrate temperature, gas ion concentration, insulating resist type and thickness, and humidity on the growth process for example is not known. The ultimate level of precision or conductivity that can be reached is also not known.

Chapter VII

Conclusion and Outlook

Section 1: A new material transport and collection approach is demonstrated, which supports the localized collection of airborne particles at a higher rate than previously possible. Specifically, we have discovered a collection mechanism that allows the localized collection of airborne particles at high rates. Strongly simplified the process is an electrodynamic Coulomb force directed transport process. The mechanism, as far as it is understood, is based on the interplay between high mobility gas ions with airborne particles, a patterned substrate, and a carrier gas. The process leads to localized collection of airborne particles at predetermined locations. The locally observed collection rate was at least 3 orders of magnitudes faster than conventional diffusion based transport. This abnormally high rate is real and finds applications in various fields.

From an application point of view, future study will focus on "active matrix based collection of airborne analytes", which describes a generic approach to collect airborne analytes in an active matrix type fashion on chip sized substrates. The fundamental study will guide us in the design of the recording chip; we anticipate improvements in the array size, minimal spot size, and concentration factors. Finally, it is possible to extend the range of analyte particles to include airborne pathogens within the field of aerobiology. In preparation for the proposal we have conducted first experiments with airborne Bacteriophages.

Section 2: The gas phase electrodeposition process is a recently discovered localized material growth/deposition process which uses charged and patterned insulators to attract or deflect an incoming flux of charged particles and gas ions in a gaseous environment. The process is more material efficient when compared to conventional vapor deposition since the material is directed to the point of use. No lift off is required. As a new application, the localized growth of freestanding three dimensional point-to-point electrical connections is demonstrated. This application requires electrically conductive and mechanically stable interconnects which has been a major challenge to the field since the

structures are composed of aggregated nanoparticles. This challenge has been solved through a size reduction of the primary particles to the sub 3 nm range. Specifically, a carrier gas was discovered as an important parameter to reduce the primary particle size below a 3 nm threshold. Moreover, the carrier gas reduced in-flight-aggregation which in turn improved the density, mechanical, and electrical property of the growing nanostructures. Due to the improved mechanical and electrical characteristics it was possible to report on the electrical properties of the growing structures for the first time.

We discovered a nearest neighbor coupling effect which supports the growth of bridges. The growth of bridges is possible due to an increased screening length when compared to the wet chemical counterpart where a high ion concentration screens charges within a few nm. Nearest neighbor coupling across a 10 μm gaps is possible. This finds applications: (i) The gas phase electrodeposition is applied to grow self-aligned free-standing nanowire based interconnects. The interconnects can connect distant points with each other in a programmable fashion through the control of the dissipation current. (ii) The formation and self-aligned growth is also used to grow an interdigitated electrode array. Here nanowire bridges grow across the rows and columns. No electrical shorts between the columns and rows were detected indicating that the crossovers are not in contact with the electrodes underneath.

In the future it should be possible to extend this further. It is possible to create turly 3D free-standing nanowire structures and freeform wire connection between disparate “off chip” parts of a system. The formation of vias between device layers through gas phase deposition should also be possible.

Bibliography

[1] J. Fang, S.-C. Park, L. Schlag, T. Stauden, J. Pezoldt and H. O. Jacobs, Adv. Funct. Mater., vol. 24, 2014.

[2] J. Fang, S.-C. Park, L. Schlag, T. Stauden, J. Pezoldt and H. O. Jacobs, Adv. Mater., vol. 26, pp. 7600-7607, 2014.

[3] J. Fang, L. Schlag, S.-C. Park, T. Stauden, J. Pezoldt, P. Schaaf and H. O. Jacobs, Adv. Mater., vol. 28, no. 9, pp. 1770-1779, 2015.

[4] C. R. Barry, J. Gu and H. O. Jacobs, Nano Lett., vol. 5, p. 2078, 2005.

[5] C. R. Barry and H. O. Jacobs, Nano Lett., vol. 6, no. 12, pp. 2790-2796, 2006.

[6] J. J. Cole, E.-C. Lin, C. R. Barry and H. O. Jacobs, Appl. Phys. Lett., vol. 95, p. 113101, 2009.

[7] J. J. Cole, E.-C. Lin, F. Johnson, J. Fang and H. O. Jacobs, Proc. NSF CMMI Grantees Conference, 2011.

[8] J. J. Cole, E.-C. Lin, C. R. Barry and H. O. Jacobs, Small, vol. 6, p. 1117, 2010.

[9] E.-C. Lin, J. J. Cole and H. O. Jacobs, Nano Lett., vol. 10, no. 11, pp. 4494-4500, 2010.

[10] E.-C. Lin, J. Fang, S.-C. Park, T. Stauden, J. Pezoldt and H. O. Jacobs, Adv. Mater., vol. 25, no. 26, pp. 3554-3559, 2013.

[11] K. Ikebukuro, C. Kiyohara and K. Sode, Biosens. Bioelectron., vol. 20, pp. 2168-2172, 2005.

[12] P. Krebs and A. Grisel, Sens. Actuators, vol. 13, pp. 155-158, 1993.

[13] T. Wagner, S. Haffer, C. Weinberger, D. Klaus and M. Tiemann, Chem. Soc. Rev., vol. 42, p. 4036, 2013.

[14] Y. Y. Vengerov and T. E. Semenov, Electron Microsc. Res., vol. 2, p. 193, 1992.

[15] E. Hao and G. C. Schatz, J. Chem. Phys, vol. 120, p. 357, 2004.

[16] J. Ji, Z. Zhou, X. Yang, W. Zhang, S. Sang and P. Li, Small, vol. 9, p. 3014, 2013.

[17] H. O. Jacobs and G. M. Whitesides, Science, vol. 291, p. 1763, 2001.

[18] A. M. Welle and H. O. Jacobs, Appl. Phys. Lett., vol. 87, p. 263119, 2005.

[19] F. Favier, E. C. Walter, M. P. Zach, T. Benter and R. M. Penner, Science, vol. 293, no. 5538, pp. 2227-2231, 2001.

[20] F. Shen, J. Wang, Z. Xu, Y. Wu, Q. Chen, X. Li, X. Jie, L. Li, M. Yao, X. Guo and T. Zhu, Nano Lett., vol. 12, pp. 3722-3730, 2012.

[21] M. D. Ward and D. A. Buttry, Science, vol. 249, no. 4972, pp. 1000-1007, 1990.

[22] M. S. Arnold, P. Avouris, Z. Pan and Z. Wang, J. Phys. Chem., vol. 107, pp. 659-663, 2003.

[23] B. Ilic, D. Czaplewski, H. G. Craighead, P. Neuzil, C. Campagnolo and C. Batt, Appl. Phys. Lett., vol. 77, p. 450, 2000.

[24] K. Besteman, J.-O. Lee, F. G. M. Wiertz, H. A. Heering and C. Dekker, Nano Lett., vol. 3, no. 6, pp. 727-730, 2003.

[25] E.-C. Lin, J. Fang, S.-C. Park, F. W. Johnson and H. O. Jacobs, Nat. Commun., vol. 4, p. 1636, 2013.

[26] K. B. Biggs, J. P. Camden, J. N. Anker and R. P. V. Duyne, J. Phys. Chem. A, vol. 113, p. 4581, 2009.

[27] M. Li, H. X. Tang and M. L. Roukes, Nat. Nanotechnol., vol. 2, p. 114, 2007.

[28] M. Tsutsui, M. Taniguchi, K. Yokota and T. Kawai, Nat. Nanotechnol., vol. 5, p. 286, 2010.

[29] C. Kanaoka, H. Emi and W. Tanthapanichakoon, AlChE J., vol. 29, no. 6, pp. 895-902, 1983.

[30] J. P. Black, A. Elium, R. M. White, M. G. Apte, L. A. Gundel and R. Cambie, IEEE Ultrasonics Symp., vol. 476, 2007.

[31] B. B. Yellen and G. Friedman, Adv. Mater., vol. 16, no. 2, p. 111, 2004.

[32] E. Verveniotis, A. Kromka, M. Ledinský, J. Čermák and B. Rezek, Nanoscale Res. Lett., vol. 6, no. 1, p. 144, 201.

[33] P. P. Tsai, H. Schreuder-Gibson and P. Gibson, J. Electrostat., vol. 54, p. 333, 2002.

[34] J. B. Fenn, M. Mann, C. K. Meng, S. F. Wong and C. M. Whitehouse, Science, vol. 246, p. 64, 1989.

[35] P. Mesquida and A. Stemmer, Adv. Mater., vol. 13, p. 1395, 2001.

[36] K. Yanallah and F. Pontiga, Plasma Sources Sci. Technol., vol. 21, p. 045007, 2012.

[37] M. Abdel-Salam, M. Nakano and A. Mizuno, J. Phys. D: Appl. Phys., vol. 40, p. 3363, 2007.

[38] S. S. Bamji, A. T. Bulinski and K. M. Prasad, IEEE Trans. Electr. Insul., vol. 104, p. 3563, 2000.

[39] L.-J. Wan, M. Terashima, H. Noda and M. Osawa, J. Phys. Chem. B, vol. 104, p. 3563, 2000.

[40] P. Schwartz, F. Schreiber, P. Eisenberger and G. Scoles, Surf. Sci., vol. 423, p. 208, 1999.

[41] L. H. Dubois, B. R. Zegarski and R. G. Nuzzo, J. Chem. Phys., vol. 98, p. 678, 1993.

[42] F. Favier, E. C. Walter, M. P. Zach, T. Benter and R. M. Penner, Science, vol. 293, p. 2227, 2001.

[43] N. Jalili and K. Laxminarayana, Mechatronics, vol. 8, p. 907, 2004.

[44] C. J. Benmore, ISRN Mater. Sci., vol. 2012, p. 852905, 2012.

[45] P. L. Stiles, J. A. Dieringer, N. C. Shah and R. P. V. Duyne, Annu. Rev. Anal. Chem., vol. 1, p. 601, 2008.

[46] J. Jang, D. Akin, K. S. Lim, S. Broyles, M. R. Ladisch and R. Bashir, Sens. Actuators, B, vol. 121, p. 560, 2007.

[47] J.-S. Chang, P. A. Lawless and T. Yamamoto, IEEE Trans. Plasma Sci., vol. 19, p. 1152, 1991.

[48] L. A. Dick, A. D. McFarland, C. L. Haynes and R. P. V. Duyne, J. Phys. Chem. B, vol. 106, p. 853, 2002.

[49] G. Harman and J. Albers, IEEE Trans. Parts, Hybrids, Packag., vol. 13, p. 406, 1977.

[50] K. Toyozawa, K. Fujita, S. Minamide and T. Maeda, IEEE Trans. Compon., Hybrids, Manuf. Technol., vol. 13, p. 667, 1990.

[51] A. C. Fischer, J. G. Korvink, N. Roxhed, G. Stemme, U. Wallrabe and F. Niklaus, J. Micromech. Microeng., vol. 23, p. 083001, 2013.

[52] C. E. Tan, J. Y. Liong, J. Dimatira, L. W. Kok, J. Tan, L. H. Wijaya and K. H. Kwong, Electronics Packaging Technology Conference (EPTC), vol. 16, p. 107, 2014.

[53] T. N. Theis, IBM J. Res. Dev., vol. 44, p. 379, 2000.

[54] S. J. Ok, C. Kim and D. F. Baldwin, IEEE Trans. Adv. Packag., vol. 26, p. 302, 2003.

[55] B.-J. d. Gans, P. C. Duineveld and U. S. Schuber, Adv. Mater., vol. 16, p. 203, 2004.

[56] Z. Fan, J. C. Ho, T. Takahashi, R. Yerushalmi, K. Takei, A. C. Ford, Y.-L. Chueh and A. Javey, Adv. Mater., vol. 21, p. 3730, 2009.

[57] J. Mei, M. R. Lovell and M. H. Mickle, IEEE Trans. Electron. Packag. Manuf., vol. 28, p. 265, 2005.

[58] J. Bharathan and Y. Yang, Appl. Phys. Lett., vol. 72, p. 2660, 1998.

[59] L. Wang and J. Liu, ECS J. Solid State Sci. Technol., vol. 4, p. 3057, 2015.

[60] J. H. Kim, W. S. Chang, D. Kim, J. R. Yang, J. T. Han, G.-W. Lee, J. T. Kim and S. K. Seol, Adv. Mater., vol. 27, p. 4322, 2015.

[61] B. W. An, K. Kim, H. Lee, S.-Y. Kim, Y. Shim, D.-Y. Lee, J. Y. Song and J.-U. Park, Adv. Mater., vol. 27, p. 4322, 2015.

[62] B. M. Smirnov, Physics of Ionized Gases, New York, NY: Wiley, 2001.

[63] S. W. Boettcher, J. M. Spurgeon, M. C. Putnam, E. L. Warren, D. B. Turner-Evans, M. D. Kelzenberg and N. S. Lewis, Science, vol. 327, p. 5962, 2010.

[64] G. A. Sehmel, US Patent 3879986, 1975.

[65] S. Biswas, Master Thesis, Lund University, 2013.

[66] N. Srivastava and K. Banerjee, IEEE/ACM International Conference, pp. 383-390, 2005.

[67] R. He and P. Yang, Nat. Nanotechnol., vol. 1, pp. 42-46, 2006.

[68] S.-K. Lee, H.-J. Choi, P. Pauzauskie, P. Yang, N.-K. Cho, H.-D. Park, E.-K. Suh, K.-Y. Lim and H.-J. Lee, Phys. Stat. Sol. (b), vol. 241, pp. 2775-2778, 2004.

[69] P.-C. Chang, Z. Fan, D. Wang, W.-Y. Tseng, W.-A. Chiou, J. Hong and J. G. Lu, Chem. Mater., vol. 16, pp. 5133-5137, 2004.

[70] M. S. Islam, S. Sharma, T. I. Kamins and R. S. Williams, Nanotechnol., vol. 15, pp. L5-L8, 2004.

[71] N. Chiodarelli, S. Masahito, Y. Kashiwagi, Y. Li, K. Arstila, O. Richard, D. J. Cott, M. Heyns, S. D. Gendt, G. Groeseneken and P. M. Vereecken, Nanotechnol., vol. 22, p. 085302, 2011.

[72] B. Tian, P. Xie, T. Kempa, D. Bell and C. Lieber, Nat. Nanotechnol, vol. 4, pp. 824-829, 2009.

[73] P. L. McEuen, M. S. Fuhrer and H. Park, IEEE Trans. Nanotechnol. 1, pp. 78-85, 2002.